Neuron

Article

Localized APP expression results in progressive network dysfunction by disorganizing spike timing

Graphical abstract

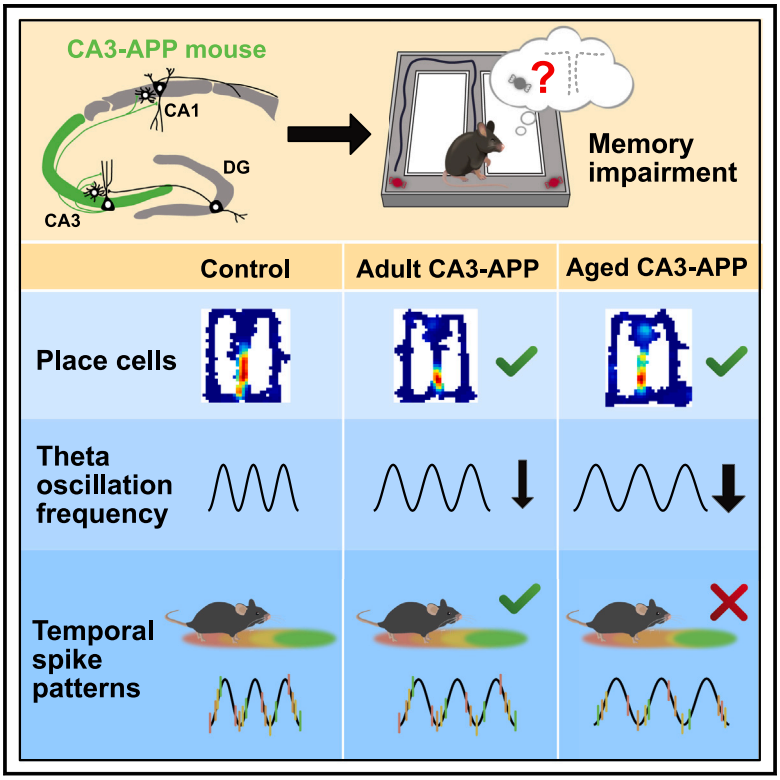

Highlights

- Expression of human mutant APP in CA3 was sufficient to result in memory impairment
- Spatial firing patterns of hippocampal CA1 and CA3 cells were largely preserved
- Hippocampal CA1 principal neurons and interneurons showed reduced theta frequency
- Impaired sequential firing of place cells best correlated with memory decline

Authors

Silvia Viana da Silva, Matthias G. Haberl, Kshitij Gaur, ..., Edward H. Koo, Jill K. Leutgeb, Stefan Leutgeb

Correspondence

jleutgeb@ucsd.edu (J.K.L.), sleutgeb@ucsd.edu (S.L.)

In brief

Viana da Silva et al. show that cognitive decline in Alzheimer's disease is not only caused by spreading pathology but also that local pathology is sufficient to result in memory dysfunction and aberrant rhythmic firing patterns in brain regions that receive projections from cells that express mutant human amyloid precursor protein.

Viana da Silva et al., 2024, Neuron *112*, 124–140
January 3, 2024
https://doi.org/10.1016/j.neuron.2023.10.001

CellPress

CellPress
OPEN ACCESS

Neuron

Article

Localized APP expression results in progressive network dysfunction by disorganizing spike timing

Silvia Viana da Silva,[1,2] Matthias G. Haberl,[3] Kshitij Gaur,[1] Rina Patel,[1] Gautam Narayan,[1] Max Ledakis,[1] Maylin L. Fu,[1] Miguel de Castro Vieira,[3] Edward H. Koo,[4] Jill K. Leutgeb,[1,*] and Stefan Leutgeb[1,5,6,*]

[1]Neurobiology Department, School of Biological Sciences, University of California, San Diego, La Jolla, CA, USA
[2]NeuroCure Excellence Cluster and German Center for Neurodegenerative Diseases (DZNE), Berlin, Germany
[3]Charité – Universitätsmedizin Berlin, Corporate Member of Freie Universität Berlin and Humboldt-Universität zu Berlin, Neuroscience Research Center, Charitéplatz 1, 10117 Berlin, Germany
[4]Department of Neurosciences, School of Medicine, University of California, San Diego, La Jolla, CA, USA
[5]Kavli Institute for Brain and Mind, University of California, San Diego, La Jolla, CA, USA
[6]Lead contact
*Correspondence: jleutgeb@ucsd.edu (J.K.L.), sleutgeb@ucsd.edu (S.L.)
https://doi.org/10.1016/j.neuron.2023.10.001

SUMMARY

Progressive cognitive decline in Alzheimer's disease could either be caused by a spreading molecular pathology or by an initially focal pathology that causes aberrant neuronal activity in a larger network. To distinguish between these possibilities, we generated a mouse model with expression of mutant human amyloid precursor protein (APP) in only hippocampal CA3 cells. We found that performance in a hippocampus-dependent memory task was impaired in young adult and aged mutant mice. In both age groups, we then recorded from the CA1 region, which receives inputs from APP-expressing CA3 cells. We observed that theta oscillation frequency in CA1 was reduced along with disrupted relative timing of principal cells. Highly localized pathology limited to the presynaptic CA3 cells is thus sufficient to cause aberrant firing patterns in postsynaptic neuronal networks, which indicates that disease progression is not only from spreading pathology but also mediated by progressively advancing physiological dysfunction.

INTRODUCTION

Alzheimer's disease (AD) is a neurodegenerative disorder characterized by progressive cognitive decline. In particular, spatial navigation is impaired early in human AD patients and has emerged as a potential cognitive biomarker to detect AD at preclinical stages.[1,2] Importantly, the early deficits in spatial navigation are not only relevant as a diagnostic strategy but also commensurate with the finding that brain circuits that support navigation, such as the hippocampus and entorhinal cortex,[3] are particularly impaired early in the disease. Aberrant firing patterns have, in turn, been shown to accelerate disease progression,[4] and restoring dysfunction in these regions is therefore a particularly urgent target for treatment approaches.

Expressing proteins with mutations found in familial forms of AD causes wide-ranging synaptic and spatial memory deficits in mice, and it is well established that synaptic dysfunction, deterioration of synapse structure, and memory impairment emerge before plaque disposition.[5–7] There is also evidence for early hyperactivity in the hippocampus in advance of plaque pathology.[8] Yet, it is not well understood how these early functional deficits progress to network dysfunction that causes memory deficits, particularly at disease phases when the release of soluble fragments of APP, including various forms of Aβ, is prevalent.[8–11] The majority of studies that address network dysfunction have been done in models of AD in which synapse loss,[12–14] deposition of amyloid-beta plaques,[15–17] or the emergence of neurofibrillary tangles is advanced.[18,19] Rodent models at advanced stages of amyloid or tau deposition display behavioral deficits along with deteriorated spatial properties of place cells in the hippocampus[15,16,19,20] and grid cell in the entorhinal cortex,[16,21,22] but there is generally no causal link as spatial coding deficits can emerge at a different time in disease progression than behavioral deficits.

In addition to the outstanding question of which emerging network dysfunction leads to the initial memory deficits in early disease stages (i.e., before extensive plaque formation and cell death), it is also not known whether broadening dysfunction emerges predominantly from the spreading molecular pathology across brain regions or can also be initiated by sustained local pathology, such as at the chronic release of APP fragments, including Aβ, from synaptic terminals. These possibilities cannot be distinguished with models of pan-neuronal APP expression, which show initial pathology, including amyloid deposition, in a few cortical areas that then increasingly broadens across brain regions.[23] Even in disease models that initially restrict APP or Tau expression to the entorhinal cortex, progressive broadening of pathology to other brain regions occurs because the

expression of the transgene spreads to other brain regions.[23,24] To distinguish between circuit dysfunction that emerges from increased broadening of APP expression across brain regions as opposed to prolonged local release of APP fragments on synaptic function, we used transgenic mice in which the expression of mutant human amyloid precursor protein (hAPP) remained selective for hippocampal CA3 pyramidal cells throughout the lifespan (CA3-APP mice). The CA3-APP mouse model shows no cell death in the hippocampus and only rare plaques in CA1 at advanced ages and thus constitutes a model to investigate the earliest features of AD-related dysfunction.[25]

Using the CA3-APP mice allowed us to determine whether local AD synaptic and cellular deficits eventually lead to dysfunction in non-APP-expressing neuron populations that are critical for supporting spatial navigation. By testing the mice at two different age points, we were able to determine that the localized hAPP expression resulted in dysfunctional network oscillations in a broader network, including in the hippocampal CA1 area, which receives projections from CA3 and does itself not express hAPP. The aberrant oscillations were accompanied by memory deficits and by altered temporal firing patterns of individual principal cells and of interneurons, but spatial firing patterns remained largely intact. This shows that altered network function progressively emerged in cell populations that are targeted by synapses from hAPP-expressing cells and that disease progression can thus be driven by sustained synaptic dysfunction. These findings also further support the idea that memory dysfunction in AD can be improved by restoring brain oscillations.

RESULTS

To test the effects of localized pathology on behavioral and circuit dysfunction, we generated mice that selectively expressed mutant hAPP in CA3 principal cells (Figures 1A and 1B; Table S1). The selective expression of the transgene in only hippocampal CA3 cells allowed for the examination of neuronal firing patterns in CA1, which does itself not express hAPP but receives direct projections from hAPP-expressing CA3 cells. We investigated the mice at two different time points of the amyloid pathology progression, at 4–6 months (young adults) and at 16–18 months (aged). We observed that the transgene was expressed in 74.5% ± 2.2% of CA3 principal cells in aged adult mice (Figures S1A–D), having previously shown that the transgene was expressed in close to 60% of CA3 cells by 6 months.[25] No plaques were observed in our mice at any age point and, in line with previous observations,[25] no APP expression was seen outside of the CA3 region in brain sections from young adult and aged mice (Figures S1A–S1C).

CA3-APP mice displayed deficits in hippocampus-dependent spatial navigation

To test whether localized APP expression in the hippocampal CA3 area was sufficient to cause a memory deficit, we trained mice to perform a spatial alternation task in a figure-8 maze (Figures 1C and 1D). This task is hippocampus dependent, with a brief delay in the central arm,[26] while a version without delay is not hippocampus dependent, thus controlling for general motor deficits. We first tested mice for 5 days before any surgical procedures to ensure that differences were not arising from inflammatory processes related to surgery.[27] CA3-APP mice performed at control levels in the continuous hippocampus-independent version of the task (Figures 1E and 1F). In the hippocampus-dependent version with a delay of 2 or 10 s, the performance was impaired in young adult and, more markedly, in aged CA3-APP mice (young adult: $p = 0.020$ and 0.0007; aged: $p = 0.001$ and $p < 0.0001$ for 2- and 10-s delay, Sidak's post hoc test; Figures 1E, 1F, and S1E–S1I).

Activity patterns of CA1 principal cells and interneurons were altered by APP expression in CA3 principal cells

We next aimed to understand whether neuronal activity in the behavioral task was altered by hAPP expression in CA3 and, if so, how pathological activity might be correlated with the memory impairments. In particular, we investigated whether APP expression resulted in a network dysfunction in cell populations that are postsynaptic to the cells with amyloid pathology. We therefore recorded from the hippocampal CA1 area (Figure S2A). The recordings were performed during an additional 10 days of testing in the spatial alternation task (Figure 1D) and were from putative principal cells and interneurons (see Figures S2B and S2C for cluster quality and classification) and also included the local field potential (LFP). During behavioral sessions while recording, young adult CA3-APP mice performed at control levels, while aged CA3-APP mice continued to be impaired with both the 2- and 10-s delay (young adult: $p = 0.083$ and 0.058, aged: $p = 0.0008$ and $p < 0.0001$, Sidak's post hoc test, Figures S1F–S1I). Control as well as transgenic mice showed improved performance across experimental days in both age groups (slopes were different from zero, Figures 1E and 1F; see also Table S2). In summary, young adult CA3-APP mice thus displayed only a transient memory deficit, while aged CA3-APP mice showed a lasting impairment in spatial memory.

We next analyzed the firing properties of CA1 principal cells and began with the average firing rate throughout the entire recording session, which included rest periods and running in the maze in all three delay conditions. Young adult CA3-APP mice showed a small reduction in the average firing rate of putative CA1 principal cells, and aged CA3-APP mice showed a more pronounced reduction ($p = 0.0048$ and 0.0006, Mann-Whitney [MW] test, Figures 2A and 2B). Despite these rate differences, the percentage of active cells in the maze (firing rate > 0.1 Hz) was similar to age-matched controls in young adult ($p = 0.997$, two-sample t test) and aged mice ($p > 0.999$, MW test, Figure 2C). The average velocity of control and CA3-APP mice when running in the maze was similar to age-matched controls in both age groups, but we found a small reduction in the velocity of young adult CA3-APP mice compared with age-matched controls during rest periods (Figures S3A and S3B). Because velocity and brain state can affect the firing rate of neurons, we therefore repeated the analysis of firing rate with only data while running in the maze, where no differences in velocity were found. We again observed reduced firing rates in young and aged CA3-APP mice compared with age-matched controls (Figures S3C, S4A, and S4B; Tables S5 and S6). These results confirmed that the reduction in firing rate is independent of behavior. We then analyzed the burst activity of CA1 principal cells during

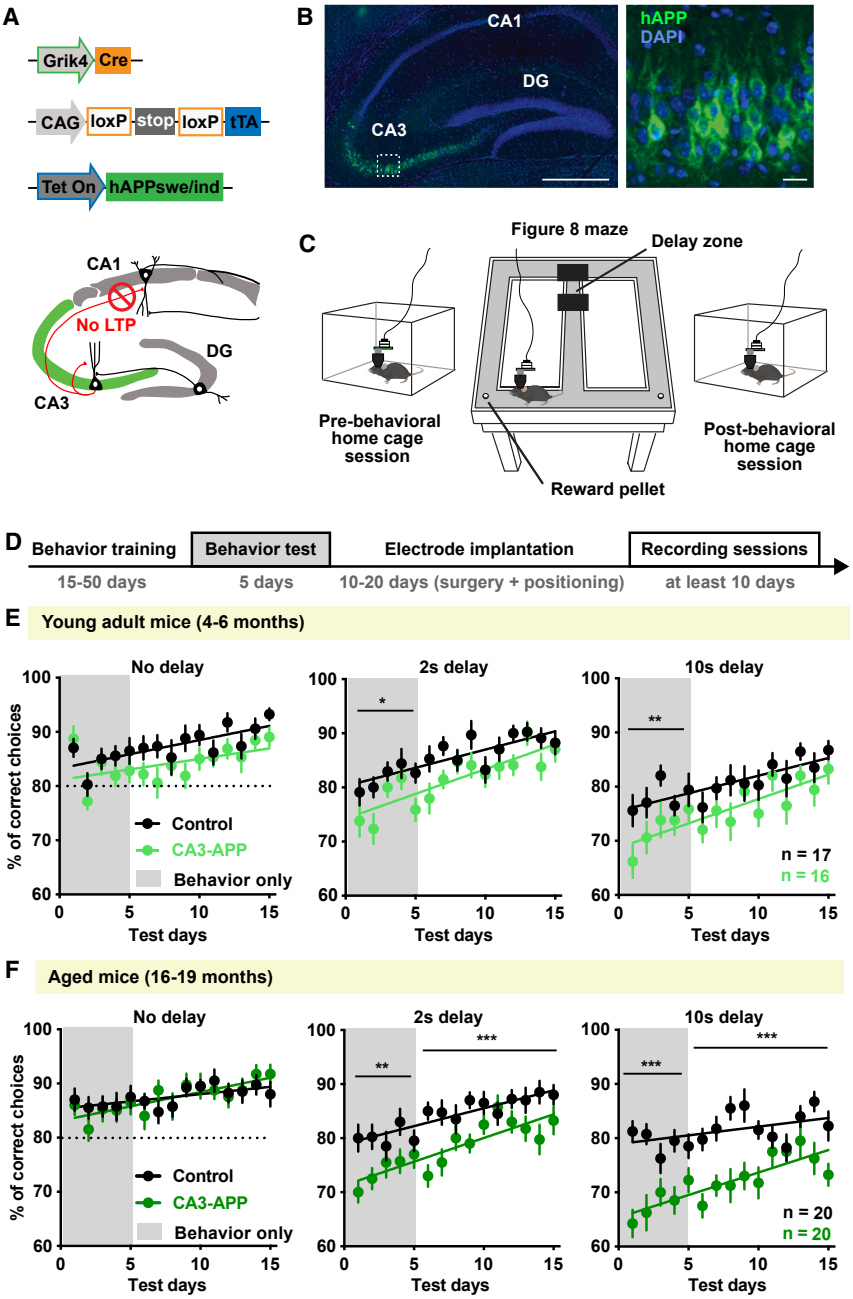

Figure 1. Hippocampus-dependent memory was impaired in CA3-APP mice

(A) CA3-APP mice carried three transgenes: (i) Cre-recombinase under the regulation of the Grik4 promoter for CA3 specificity, (ii) a tetracycline-controlled transactivator protein (tTA) transgene under the control of Cre-LoxP recombination, and (iii) the hAPP mutant gene under the control of a tetracycline-responsive promoter element (TRE). LTP of Schaffer-collateral inputs to CA1 is impaired in CA3-APP mice starting at 4 months of age.[25]

(B) Example immunostaining of a section from an aged CA3-APP mouse in which recordings were taken in the same hemisphere. Anti-hAPP (6E10 antibody), green; DAPI, blue. Scale bars: 0.5 mm (left) and 20 μm (right).

(C) Recording paradigm included 30 laps in the figure-8 maze, preceded and followed by a 10–15-min baseline session in the home cage.

(D) Experimental timeline.

(E) Behavioral performance over experimental days for young adult CA3-APP mice (n = 16) and littermate controls (n = 17). During the initial 5 days of behavior testing with delays, there was a reduction in correct choices by CA3-APP mice compared with age-matched controls (two-way RM ANOVA, p = 0.020 and 0.0007 for 2- and 10-s delay, Sidak's post hoc test). This difference was not observed on subsequent recording days (two-way RM ANOVA, p = 0.058 and 0.079 for 2- and 10-s delay, Sidak's post hoc test; see Figures S1F and S1G). Performance improved over time in each delay condition (see linear regression analysis in Table S2) for both experimental groups.

(F) Behavioral performance over experimental days for aged CA3-APP mice (n = 20) and littermate controls (n = 20). In the delayed versions of the task, CA3-APP mice made fewer correct choices than age-matched controls, both during the initial 5 days of testing (two-way RM ANOVA, p = 0.001 and p < 0.0001 for 2- and 10-s delay, Sidak's post hoc test) and during the recording period (two-way RM ANOVA, p = 0.0008 and p < 0.0001 for 2- and 10-s delay, Sidak's post hoc test; see Figures S1H and S1I). The performance of all experimental mice improved over time in all delay conditions (see linear regression analyses in Table S2). For (E) and (F), symbols with error bars correspond to the mean ± SEM of all mice in a group. *p < 0.05, **p < 0.01, ***p < 0.001.

the task and identified a reduction in young adult, but not in aged, CA3-APP mice compared with age-matched controls (p < 0.0001 and p = 0.21, MW tests, Figures S3D and S4C). However, the lack of effect for the comparison between the aged groups arises from a reduction in the burst index of control principal cells in aged mice (Figure S3F).

Next, we evaluated the firing of putative CA1 interneurons recorded from young adult mice and found similar average firing rates between genotypes (Figure 2D). Although the mean firing rate of interneurons did also not differ in aged CA3-APP mice compared with age-matched controls (p = 0.36, MW test), there was a notable increase in the number of cells with abnormally low or abnormally high firing rates (p = 0.0002, Kolmogorov-Smirnov test, Figures 2D, S3E, and S3G). Hippocampal interneurons are known to be reliably speed modulated—a characteristic that could be used for updating positional information during spatial navigation.[28] Interestingly, we observed a decrease in speed modulation of CA1 interneurons during the behavioral task in both CA3-APP age groups compared with their respective controls (both p values < 0.0001, two-sample t tests, Figure 2E). Despite the decrease in speed modulation compared with controls, interneurons from young adult CA3-APP mice still retained some speed modulation (p < 0.0001 for control and CA3-APP mice, Wilcoxon signed rank tests, Figure 2E). Also,

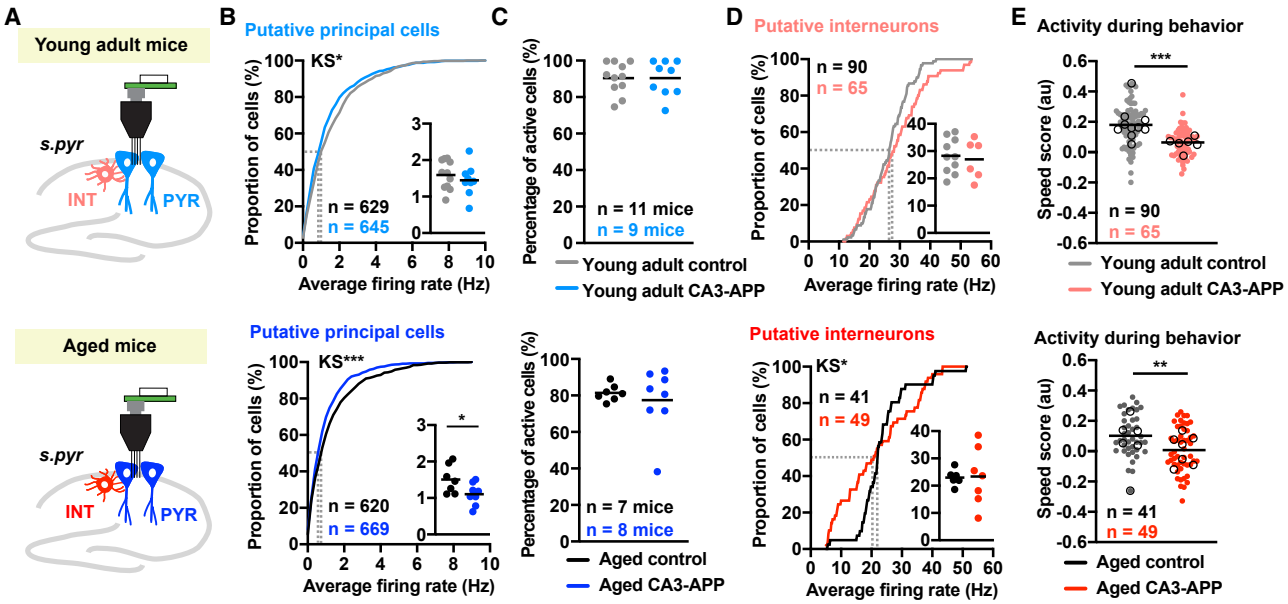

Figure 2. Firing rates of CA1 principal cells were reduced in CA3-APP mice

(A) Schematics of recordings from putative principal cells (see Figure S2C for classification). Young adult mice, upper; aged mice, lower.

(B) Cumulative distribution of average firing rate of all putative CA1 principal cells during the entire recording session (home cage and behavior). CA1 principal cells of CA3-APP mice had reduced firing rates compared with age-matched control mice (young adult: $p = 0.0048$; aged: $p = 0.0006$, MW tests). The inset shows the same data per mouse (young adult: $p = 0.45$; aged: $p = 0.041$, two-sample t tests).

(C) Percentage of cells active during the figure-8 task did not differ between CA3-APP mice and age-matched controls.

(D) Cumulative distribution of average firing rate of putative interneurons during the entire recording session. Average firing rates of CA1 interneurons did not differ between CA3-APP mice and age-matched controls (young adult: $p = 0.084$, two-sample t test; aged: $p = 0.36$, MW test). The inset graph shows the same data plotted per mouse (young adult: $p = 0.71$; aged: $p = 0.94$, two-sample t tests).

(E) The speed score of interneurons, calculated using periods of mobility in the maze, was reduced in both young adult and aged CA3-APP mice compared with age-matched controls (young adult: $p < 0.0001$; aged: $p = 0.0024$, two-sample t tests). Interneurons in young adult, but not in aged CA3-APP mice retained some speed modulation ($p < 0.0001$ and $p = 0.67$, Wilcoxon signed rank tests). Horizontal lines depict the mean of all cells in a group, and open circles the mean per mouse. All statistics are reported in Tables S3 and S4.

while interneurons in aged control mice were speed modulated, the modulation was no longer detectable in aged CA3-APP mice ($p < 0.0001$ and $p = 0.67$, Wilcoxon signed rank tests, Figure 2E). Taken together, we thus observed a decrease in the firing rate of CA1 principal cells with CA3-APP expression, which is exacerbated in aged mice. Conversely, the overall mean firing rate of interneurons remained similar across genotypes at both age points but with diminished speed modulation in young adult and, to a larger extent, in aged CA3-APP mice.

CA1 spatial activity patterns remained unaltered despite changes in firing rate

In order to identify possible mechanisms underlying the deficits in spatial memory observed in our animal model, we compared the spatial firing patterns between CA3-APP and control mice while they performed laps (i.e., from one reward location to the next) in the alternation task. We selected laps with a 10-s delay for our analysis, as this was the condition when CA3-APP mice showed the most pronounced behavioral impairment (Figures 3A and 3B). First, we asked whether there was a difference in the fraction of principal cells coding for place and found that the percentage of place cells was similar between control and CA3-APP mice for both age groups (young adult: $p = 0.27$; aged: $p = 0.87$, MW tests, Figure 3C). We then evaluated the properties of place cells that were active during the task. As expected, we found place cell coding for each segment of the maze in left-turn and right-turn laps (Figure 3B). Consistent with the reduction in mean firing rates (see Figure 2), the peak firing rate of CA1 place cells was reduced in young adult CA3-APP mice and, again to a larger extent, in aged CA3-APP mice ($p = 0.0065$ and 0.001, MW tests, Figure 3D). The spatial information carried by CA1 place cells nonetheless remained intact in CA3-APP mice at both age points ($p = 0.13$ and 0.15, MW tests, Figure 3E). However, we found that CA1 place cells in CA3-APP mice had, on average, fewer place fields when compared with control littermates (young adult: $p = 0.028$; aged: $p = 0.0083$, MW tests, Figure 3F) and that place fields in aged CA3-APP mice were slightly smaller (young adult: $p = 0.82$; aged: $p < 0.0001$, MW tests, Figure 3G) and less stable than in controls (young adult: $p = 0.57$; aged: $p = 0.015$, MW tests, Figure 3H).

To successfully perform the spatial alternation task, mice need to process information about the immediately preceding trajectory and retain the information before making the next choice. A mechanism for retaining behaviorally relevant information is trajectory-dependent firing that begins on the return arm and continues during the delay. We therefore first examined how distinct the firing patterns were between left and right sides of the maze[29,30] by computing spatial correlations between the left and right maze sections. Lower spatial correlations correspond

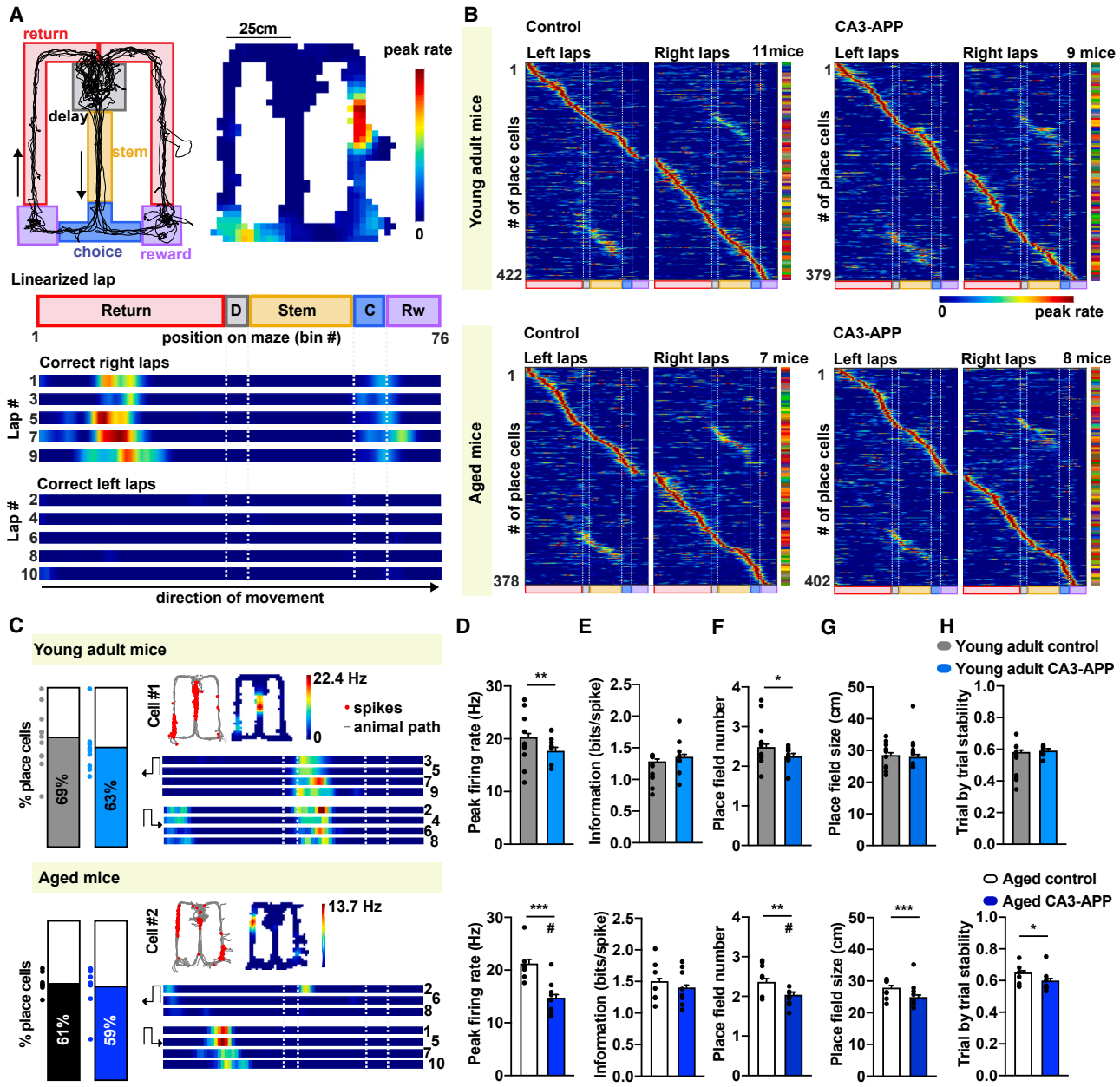

Figure 3. CA1 place code remained accurate in CA3-APP mice

(A) Left top: example of mouse path (black) and parsing of figure-eight maze into sub-sections. Direction of movement is depicted by arrows. Right top: example of a place cell recorded while the mouse ran in the maze. Spike density in two-dimensional space is averaged over all laps and shown as a color-coded map. Bottom: place cell firing is shown separately for each lap in linearized, color-coded maps (76 bins of 2.5 cm).

(B) Average linearized rate maps for all CA1 place cells recorded in the four experimental groups. Left-turn and right-turn trials are shown separately. Cells are ordered by the location of the bin with the highest firing rate. In the vertical bar to the right of each panel, cells of each individual mouse are assigned a color to show the distribution across mice.

(C) Left: % CA1 principal cells with place fields. Dots represent the same data per mouse. Right: example linearized rate maps of place cells from a young adult (top) and from an aged CA3-APP mouse (bottom).

(D) Peak firing rates of CA1 place cells were reduced in young adult and aged CA3-APP mice compared with age-matched controls (young adult: $p = 0.0065$; aged: $p = 0.001$, MW tests). In aged mice, significance was also reached when data were analyzed per mouse (indicated by #, $p = 0.0032$, $n = 7$ for control and 8 for CA3-APP mice).

(E) Information content of place cells from CA3-APP mice did not differ from age-matched control mice.

(F) The number of place fields per place cell was slightly lower in CA3-APP compared with age-matched control mice (young adult: $p = 0.028$; aged: $p = 0.0083$, MW test). For cells from aged CA3-APP mice compared with age-matched controls, the significance was also reached when data were analyzed per mouse (represented by #, $p = 0.0057$, $n = 7$ for control and 8 for CA3-APP mice).

(legend continued on next page)

to more distinct spatial coding between the two sides, and we did not find any differences in correlations compared with age-matched controls for either young adult or aged CA3-APP mice (Figure S4D), suggesting that place coding remained side-arm-selective with CA3-APP expression. Next, we examined whether the information about the preceding trajectory is retained during the delay intervals, which might support memory-guided behavior and spatial navigation.[21–23] We observed cells that fired differently in the central arm, depending on whether mice came from the left or right side and were about to perform a right or left correct turn in the maze. The percentage of turn-selective cells in CA3-APP mice did not differ from age-matched controls (young adult: $p = 0.20$; aged: $p = 0.24$, two-sample t tests), and the spatial properties in CA3-APP mice were not distinct from age-matched controls other than the reduced place field size, which was also detected in other maze segments (Figures S4E–S4H). In summary, despite rate differences, place coding remained robust in the CA1 region of CA3-APP mice.

LFP theta oscillation frequency decreased in CA3-APP mice

Because spatial coding remained accurate, even in aged CA3-APP mice with pronounced memory deficits, we next examined whether there were other functional deficits that could underlie deficits in spatial working memory. Brain oscillations are known to organize spiking activity and are linked to memory processes.[31] Using the same maze segments as for the analysis of firing rates (see Figure 3A), we analyzed hippocampal oscillations in different maze regions. For each maze region, we computed a power spectrum density (PSD) function of the normalized LFP signal and determined the peak frequency and power at defined frequency bands—delta (2–6 Hz), theta (6–12 Hz), beta (14–26 Hz), low gamma (26–50 Hz), and high gamma (50–120 Hz) (Figures 4A and S5). In analyses of oscillation frequencies, we identified a reduction in the peak frequency of theta and high-gamma oscillations ($p = 0.037$ and 0.0062, MW tests) recorded in the CA1 pyramidal layer of young adult CA3-APP mice. The quantification for the central arm of the maze (with stem and choice regions combined) is shown in Figure 4B, but similar results were obtained for other regions of the maze and when running in the home cage (Figures S5 and S6). The peak frequency of delta, beta, and low gamma oscillations was similar between control and CA3-APP mice during the memory task ($p = 0.14$, 0.074, and 0.58, MW tests), and no differences in normalized power were detected for any of the analyzed LFP bands (Figure 4C). Compared with young adult CA3-APP mice, the reduction in the frequency of theta oscillations was even more pronounced in CA1 LFP recordings of aged CA3-APP mice ($p = 0.00014$, MW test) but, again, with no differences in power (Figures 4E and 4F). High gamma oscillations were also slower in the aged CA3-APP mice ($p = 0.042$, MW test), while delta, beta, and low gamma oscillation frequencies were not different from age-matched controls ($p = 0.21$, 0.056 and 0.47, MW tests). We found a small decrease in the power of the beta band (which overlaps with the second harmonic of theta) in aged CA3-APP mice compared with age-matched controls ($p = 0.043$, MW test), which was most prominent in the central arm of the maze, particularly in the choice section (Figures 4D, 4F, and S5G). No other differences in the power of hippocampal oscillations were found in aged CA3-APP mice compared with controls (see Table S7). It is therefore predominantly the frequency of brain oscillations that is altered by CA3-APP expression, and we confirmed that these results could be obtained irrespective of a particular frequency analysis method by also analyzing the broadband signals (Figure S7).

It is important to note that aged CA3-APP mice moved slower in the choice and reward segments of the maze (Figure S6D). However, our analysis across maze segments revealed that the frequency reduction cannot be explained by differences in running speed, as lower theta and high gamma oscillation frequencies were seen in all maze segments (Figures S5 and S7), including in segments without velocity differences, such as return and stem (Figure S6C and S6D). Furthermore, we analyzed the relationship between the velocity of the mice and the frequency and power of theta oscillations in the home cage and in the behavioral task. Theta frequency differences were observed irrespective of running speed and behavior condition and, interestingly, theta oscillation frequency was less dependent on running in the spatial memory task than in the home cage. Yet, the reduction in theta frequency by hAPP expression was pronounced in the memory task in young and aged mice (Figures S6E–S6H). Taken together, the oscillation frequencies of theta and high gamma oscillations were reduced in CA3-APP mice compared with age-matched controls, irrespective of running speed.

Temporal properties of principal cells and interneurons were altered in CA3-APP mice

Because LFP oscillations reflect temporally coordinated neuronal activity of inputs to a brain region and of local circuits,[32,33] we aimed to understand whether slower theta oscillations were associated with changes in the temporal activity patterns of principal cells and interneurons in the CA1 region. We first measured the oscillation frequency of the spiking of principal cells in young adult mice. A similar percentage of cells from control and CA3-APP mice had a peak within the theta band ($p = 0.25$, Chi-square test, Figure S8A). These cells showed a decrease in the average spike oscillation frequency with CA3 hAPP expression ($p < 0.0001$, MW test, Figure 5A) but no difference in their theta modulation amplitude ($p = 0.17$, MW test, Figure 5B). As previously described,[34] the average frequency of CA1 principal cell spiking is faster than the LFP, which was also observed here for all groups of mice. However, the cells' frequencies and the ongoing LFP

(G) Place field size of CA1 place cells from aged CA3-APP mice was smaller than of cells from age-matched controls ($p < 0.0001$, MW test). In young adult CA3-APP mice, the difference was not significant ($p = 0.82$, MW test).

(H) Stability of place cells' firing was analyzed by a lap-by-lap correlation across location bins. A small reduction in stability was found in aged CA3-APP mice compared with age-matched control mice ($p = 0.015$, MW test), but no difference was observed in young adult mice ($p = 0.57$, MW test).

For (D)–(H), bar graphs represent the mean ± SEM for cell-wise analysis and black dots represent the average per mouse. All statistics are reported in Table S6.

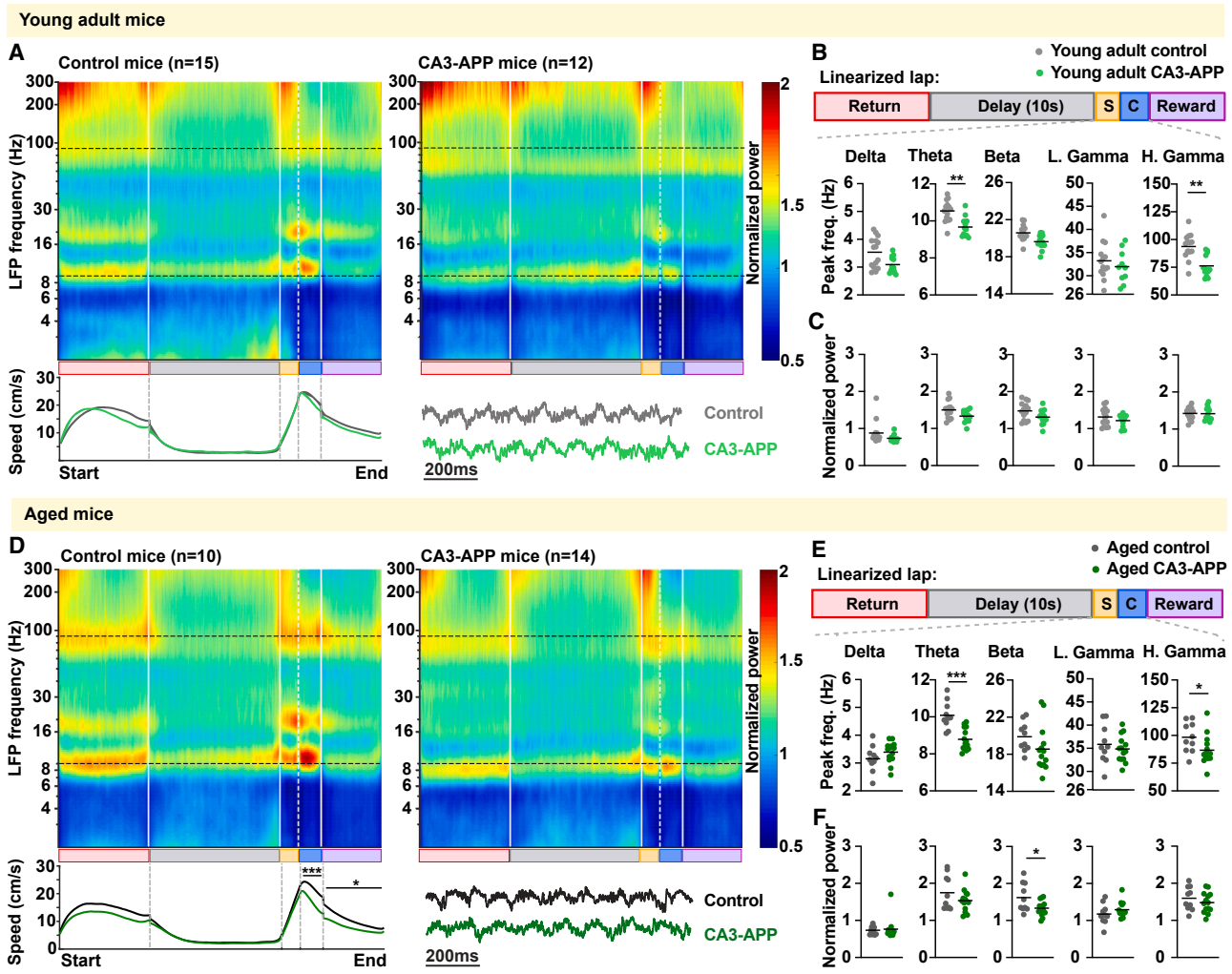

Figure 4. Theta and gamma oscillation frequencies were reduced in young adult and aged CA3-APP mice

(A) Average CA1 LFP spectrograms of young adult CA3-APP and control mice. The plot at the bottom of each panel shows the running speed of mice across different sub-sections of a lap in the figure-8 maze. Young adult CA3-APP mice (n = 15 mice) showed no difference in running speed compared with age-matched controls (n = 12 mice) in any of the maze sub-sections (Figure S6C).

(B) Quantification of frequency in different LFP bands. Quantification is shown for the center arm (including stem and choice point). Analyses for other maze sections are provided in Figure S5 and Table S7 and generally follow the same pattern. The theta and high gamma frequencies (p = 0.037 and 0.0062, MW tests adjusted for multiple comparisons by Holm-Šídák method) of young adult CA3-APP mice were reduced compared with age-matched controls.

(C) Quantification of CA1 LFP power in different frequency bands. We found no differences between young adult CA3-APP mice and their age-matched controls.

(D) Average CA1 LFP spectrograms of aged CA3-APP and control mice. Aged CA3-APP mice showed a small reduction in running speed compared with age-matched controls (n = 10 for control and n = 14 for CA3-APP mice) in only the choice and reward sections of the maze (Figure S6D). Data are displayed as in (A).

(E) Similar to young adult mice, aged CA3-APP mice showed a reduction in theta and high-gamma oscillation frequencies compared with age-matched controls (p = 0.00014 and p = 0.042, MW tests adjusted for multiple comparisons by Holm-Šídák method). Data are displayed as in (B). Detailed controls for running speed are presented in Figure S6 and Tables S8 and S9.

(F) Power in the beta band was decreased in aged CA3-APP mice compared with controls (p = 0.043, MW test adjusted for multiple comparisons by Holm-Šídák method). Data are displayed as in (C). This difference is only found in the choice zone (see Figure S5G for by-section analysis).

frequency were shifted to similar extents, such that the average frequency difference did not differ between young adult control and CA3-APP mice (p = 0.81, MW test, Figure S8A). In line with the retained frequency difference, the relationship of CA1 principal cells with the phase of ongoing theta oscillations was otherwise normal in young adult CA3-APP mice (preferred firing phase: p = 0.93; theta phase locking: p = 0.056, MW tests, Figure S8B). For CA1 interneurons in young adult mice, a similar percentage of cells from control and CA3-APP mice had spiking patterns with rhythmicity in the theta band (p = 0.11, Chi-square test), but the average frequency was lower in CA3-APP than in control mice (p = 0.0024, MW test, Figure 5C). Again, the differences between the interneurons' frequencies and the LFP frequency remained preserved with APP expression (p = 0.33, MW test, Figure S8C). A small reduction in the amplitude of theta modulation was found for CA1 interneurons in CA3-APP compared with control littermates (p = 0.0039,

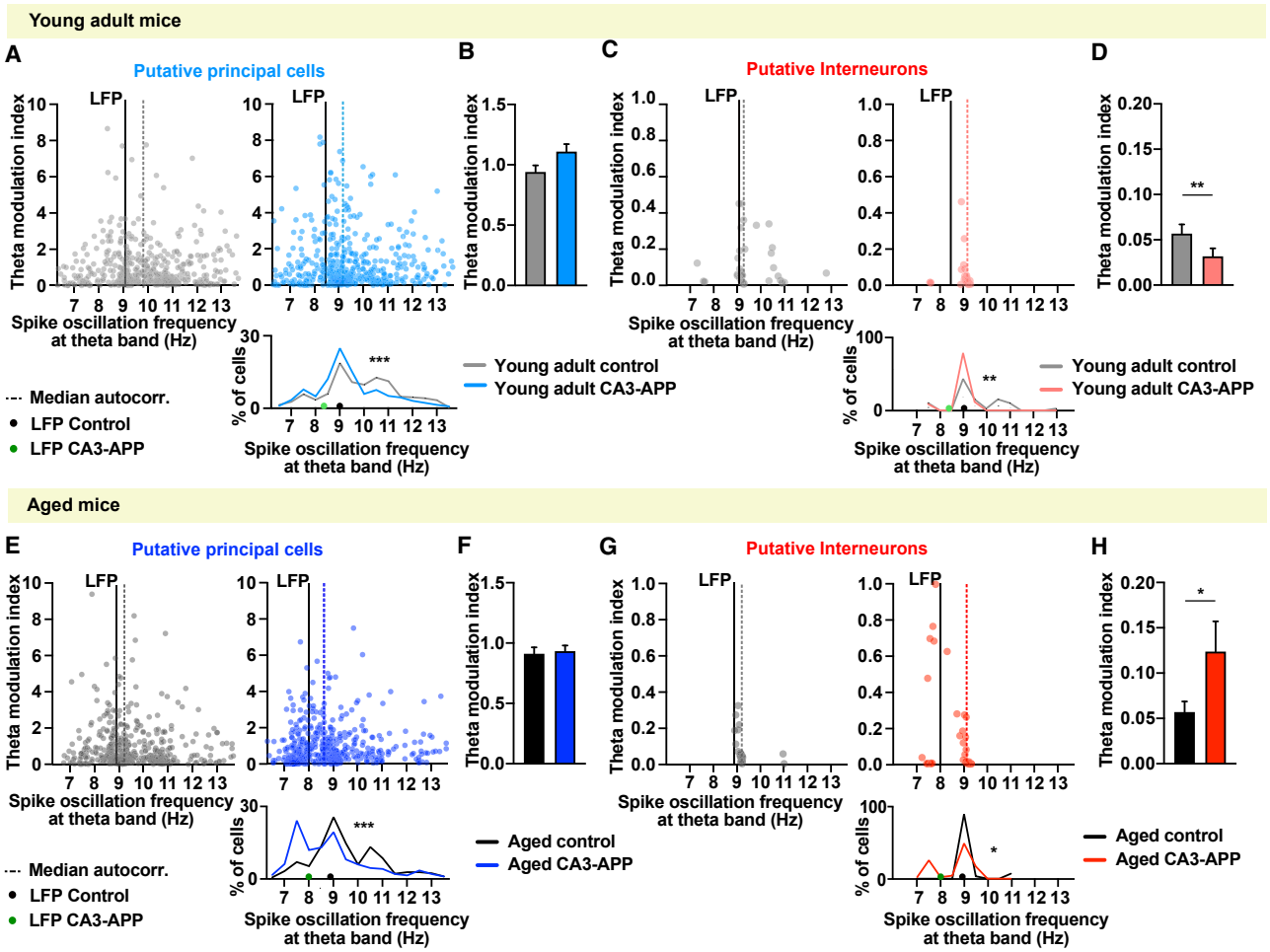

Figure 5. Spike oscillation frequency of CA1 principal cells and interneurons was reduced in CA3-APP mice

(A) For each neuron, we calculated the spike-time autocorrelation and then used fast Fourier transform analyses to obtain the predominant spike oscillation frequency. The distribution of the peak oscillation frequencies is plotted against the amplitude of their theta modulation (i.e., theta modulation index). Only cells with a detectable peak within the theta band are displayed, and the dashed line represents the median of their frequency distribution. Mean LFP frequency of the sessions in which cells were recorded, solid black line. Spike oscillation frequencies of CA1 principal cells were lower in young adult CA3-APP mice than in age-matched controls (n = 488 and 481 cells in CA3-APP and control mice, $p < 0.0001$, MW test).

(B) Average theta modulation amplitude (theta modulation index) of all active CA1 principal cells. There was no difference between young adult CA3-APP mice compared with age-matched controls (n = 554 and 561 cells, $p = 0.17$, MW test).

(C) In young adult CA3-APP mice, there were no interneurons with high spike oscillation frequencies, which resulted in a different distribution than in young adult controls (n = 34 and 39 cells, $p = 0.0024$, MW test). Data are displayed as in (A).

(D) Theta modulation amplitude of CA1 interneurons was reduced in young adult CA3-APP compared with age-matched control mice (n = 60 and 90 cells, $p = 0.0039$, MW test).

(E) When compared with age-matched controls, CA1 principal cells from aged CA3-APP mice showed a major reduction in the spike oscillation frequency, with a large fraction of cells oscillating between 7 and 8 Hz (n = 484 and 452 cells in CA3-APP and control mice, $p < 0.0001$, MW test). Data are displayed as in (A).

(F) Theta modulation amplitude of CA1 principal cells of aged CA3-APP mice did not differ from age-matched controls (n = 527 and 499 cells, $p = 0.46$, MW test).

(G) When compared with controls, CA1 interneurons from aged CA3-APP mice showed reduced spike oscillation frequencies, with >20% of interneurons now oscillating below the LFP frequency (n = 47 and 28 cells in CA3-APP and control mice, $p = 0.029$, MW test). Data are displayed as in (A).

(H) CA1 interneurons from aged CA3-APP mice showed an increase in theta modulation amplitude compared with age-matched controls (n = 50 and 41 cells, $p = 0.038$, MW test).

Bar graphs with error bars correspond to the mean ± SEM. All statistics are reported in Table S11.

MW test, Figure 5D) but without differences in phase preference or phase locking ($p = 0.40$ and 0.54, Figure S8D). Overall, in young adult mice with APP expression, there was a minor reduction of the frequency of principal cells and interneurons, but this occurred in parallel with a reduction of the LFP frequency, such that the frequency differences between the two types of oscillations were preserved.

We next analyzed the spiking patterns of aged mice. Most active CA1 principal cells had spike patterns with rhythmicity in the theta band (control vs. CA3-APP, $p = 0.48$, chi-square

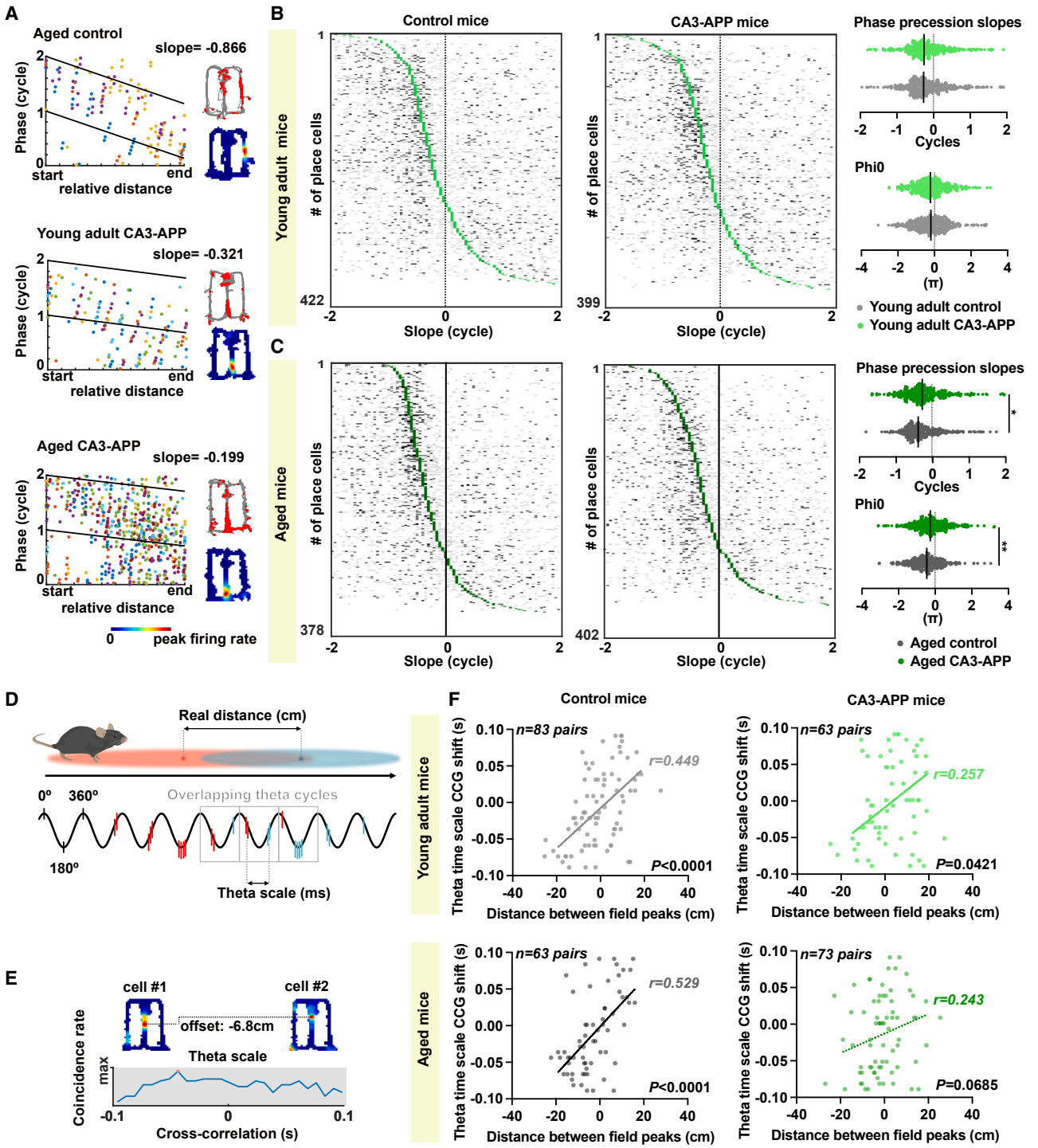

Figure 6. Phase precession and theta sequences were impaired in aged but not in young adult CA3-APP mice

(A) Phase precession slopes of example CA1 place cells. Each spike train in the phase-distance plot is depicted in a different color. Place maps of the corresponding cells are shown to the right. Top: spike locations (red dots) plotted on the mouse's path (gray line). Bottom: spike rate map, color-coded with red as the peak rate.

(B) Distribution of phase precession slopes. Each row shows the phase precession slopes of each spike train (gray ticks, non-significant; black ticks, significant) of one place cell in the figure-8 maze. The median (green tick) was calculated by including significant and non-significant slopes, and cells are ordered by their median slope. Phase precession and phase offset in young adult CA3-APP mice did not differ from age-matched controls (n = 351 and 386 cells, p = 0.097 and 0.62, MW tests).

(legend continued on next page)

test), but cells in CA3-APP mice showed a pronounced reduction in their spike oscillation frequency ($p < 0.0001$, MW test), with a subset of about 20% of the cells oscillating at frequencies as low as ~7.5 Hz (Figure 5E). Nevertheless, the distance between the preferred frequency of individual cells and the LFP frequency did on average not differ from control littermates ($p = 0.46$, MW test, Figure S8E), indicating that cells' oscillations were altered along with network oscillations. As observed in young adult CA3-APP mice, we found no differences in theta modulation amplitude ($p = 0.46$, MW test, Figure 5F), preferred phase, or phase locking of principal cells in aged CA3-APP mice compared with controls ($p = 0.90$ and 0.96, MW tests, Figure S8F). Of the CA1 interneurons from aged CA3-APP mice, 94.0% were theta modulated, in contrast with 68.3% in control mice ($p = 0.0013$, Chi-square test). Resembling the frequency patterns in CA1 principal cells, a subset of CA1 interneurons (~20%) from aged CA3-APP mice was oscillating at ~7.5 Hz. The effect was sufficiently pronounced in interneurons to result in a decrease in the average spike oscillation frequency ($p = 0.029$, MW test, Figure 5G), but the shift was less than for the LFP frequency so that the difference between the CA1 interneurons spike oscillation frequency and the LFP frequency was significantly larger in aged CA3-APP mice compared with age-matched controls ($p = 0.0003$, MW test, Figure S8G). Furthermore, we observed a substantial increase in theta modulation amplitude of CA1 interneurons in aged CA3-APP mice ($p = 0.0380$, MW test; Figure 5H). The increase in theta modulation was most pronounced in the subset of interneurons oscillating at the reduced ~7.5 Hz frequency (Figure 5G). Again, we did not find changes in preferred theta phase or phase locking ($p = 0.97$ and 0.068, MW tests; Figure S8H) of CA1 interneurons. In summary, the shift in the oscillation frequency in aged CA3-APP mice was more pronounced than in young adult CA3-APP mice and was mostly due to the appearance of a subset (~20%–30%) of both principal cells and interneurons now oscillating at a lower than normal frequency of ~7.5 Hz.

Phase precession and pairwise timing were impaired in aged CA3-APP mice

Place cells in the hippocampus are known to shift their firing to earlier phases of the theta cycle as the animal transverses the place field ("theta phase precession").[34,35] We asked whether the changes in theta-related temporal organization resulted in the reorganization of the cells' temporal firing patterns with respect to LFP and with respect to each other. To address this, we analyzed phase shifts over the course of spike trains (see STAR Methods) and found that the majority of CA1 place cells showed some level of phase precession (Figures 6A–6C). Place cells from young adult CA3-APP mice had control levels of phase precession, while aged CA3-APP mice showed a reduction in phase precession compared with age-matched controls (comparisons in young adult and aged mice, slope: $p = 0.97$ and 0.028; offset: $p = 0.62$ and 0.011, MW tests). Interestingly we only saw a reduction in phase precession when the task was hippocampus dependent (2- and 10-s delay) but not during the continuous version of the task (Figures S9A and S9B).

We then evaluated whether the reduction in phase precession during the memory task was connected to a reduced pairwise temporal organization of CA1 place cells. For pairs of simultaneously recorded cells with overlapping fields, we computed their distance on the maze (behavioral scale) and their temporal distance within a theta cycle (theta timescale). As expected when behavioral sequences correspond to time-compressed sequences within the theta cycle,[36] we saw a clear correlation between distance and theta time in young adult and aged control mice (p values < 0.0001, Spearman correlations). However, the correlation was weaker in young CA3-APP mice ($p = 0.048$) and no longer significant in aged CA3-APP mice ($p = 0.070$, Figures 6D–6F). As a consequence, the slope of the relation between theta timescale vs. behavioral scale (i.e., sequence compression) was reduced in aged CA3-APP mice (Figure S10), which indicates that sequential activation in the maze no longer consistently corresponded to the precise temporal order within the theta cycle.

Network alterations in the CA3/DG region of CA3-APP mice were not more severe than in CA1

Unlike previous studies, we performed recordings from cells that did not directly express hAPP, such that physiological deficits can be assumed to arise from dysfunctional synaptic inputs. However, the observed effects were mostly on temporal firing patterns, and it is conceivable that more severe deficits could be detected when directly recording from the neuron population with hAPP expression. We therefore next performed analyses of recordings of spatial and temporal firing patterns in the hippocampal CA3/DG regions (Figures 7A and 7D) and asked whether we could identify larger deficits. Similar to the CA1 region, we found a reduction in the LFP theta frequency in the CA3/DG region of aged CA3-APP mice ($p = 0.0029$, MW test, Figure 7E) and again a less pronounced reduction in young adult CA3-APP mice, which did not reach significance compared with age-matched control recordings ($p = 0.31$, MW test, Figure 7B). The effect in CA3/DG was nonetheless comparable with the magnitude of the effect in CA1 ($p > 0.999$, Kruskal-Wallis test with Dunn's multiple comparisons test). As for CA1 recordings, the observed differences in theta oscillation frequency were retained when controlling for running speed (Figures S6, S11,

(C) Same as in (B) but for aged CA3-APP mice. There was a reduction in phase precession slope in aged CA3-APP mice compared with age-matched controls, and the phase offset was closer to zero in CA3-APP mice compared with controls ($n = 351$ and 342 cells, $p = 0.028$ and 0.0019, MW tests).

(D) Schematic for the comparison between the spatial distance of CA1 place field peaks and the temporal distance within a theta cycle. Both measurements can be obtained from pairs of overlapping place fields.

(E) Example metrics obtained from a pair of simultaneously recorded cells with overlapping place fields. Theta timescale shift is measured as the time bin with the peak cross-correlation in the −100-ms to +100-ms interval.

(F) Correlation between place field distance and shift in theta timescale firing was found in young adult CA3-APP and control mice ($n = 63$ and 83 pairs of overlapping place fields, $p = 0.042$ and $p < 0.0001$, Spearman correlations) and in aged control mice ($n = 63$ pairs, $p < 0.0001$) but not in aged CA3-APP mice ($n = 73$ pairs, $p = 0.069$). All statistics are reported in Table S12.

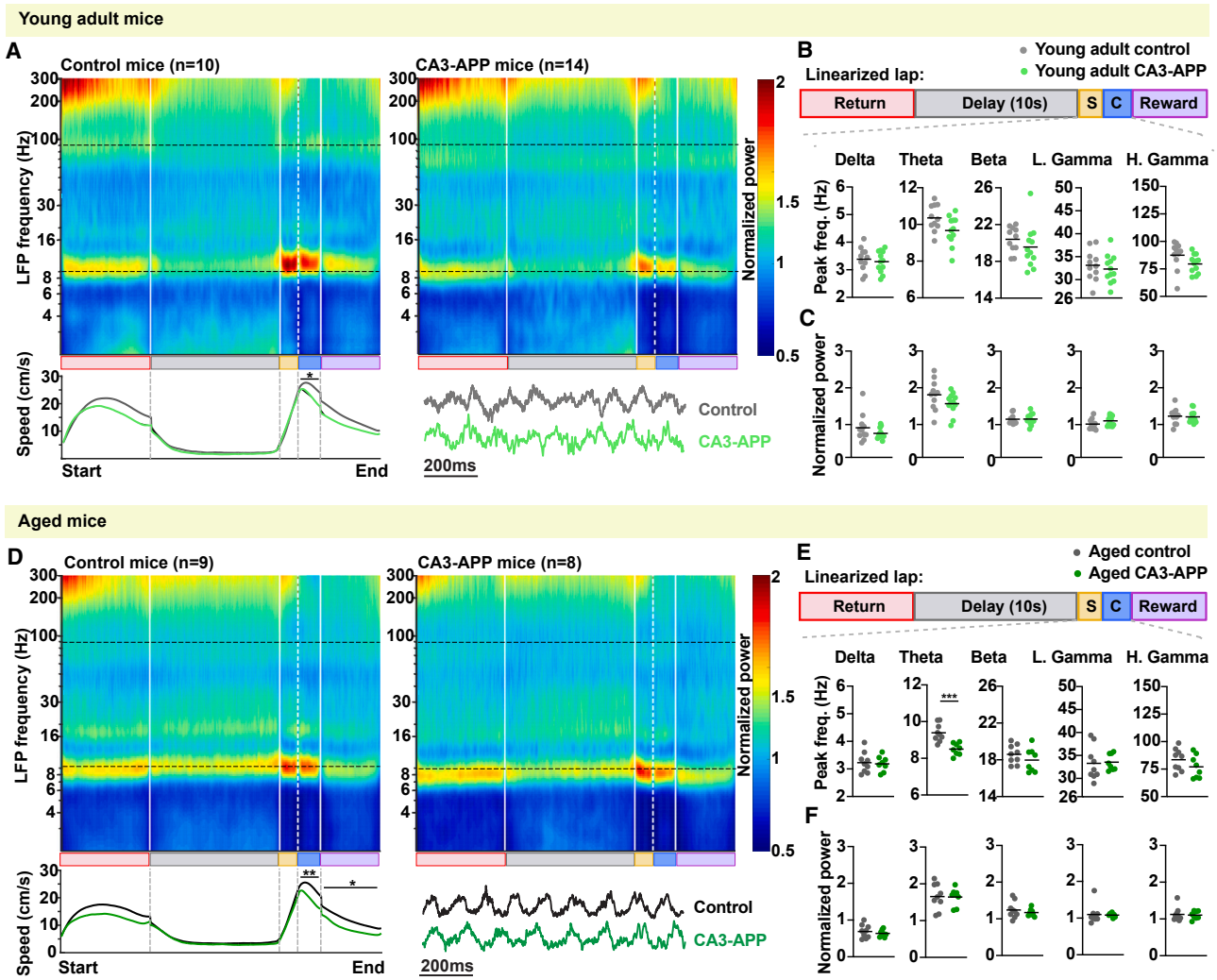

Figure 7. Recordings in CA3/DG showed lesser or comparable effects on LFP frequency compared with recordings in CA1

(A) LFP spectrograms and running speed plots for recording sites in the CA3/DG area of young adult mice are depicted as in Figure 4A. Young adult CA3-APP mice (n = 12) showed a minor difference in running speed compared with young adult control mice (n = 11 mice) in only the choice sub-section of the maze (Figure S6C).

(B) Quantification of frequency in different LFP bands is shown for the center arm (including stem and choice point). Analyses for other maze sections are provided in Figure S11 and Table S13 and generally follow the same pattern. Theta and high gamma frequencies (p = 0.31 and 0.091, MW tests adjusted for multiple comparisons by Holm-Šídák method) did not differ between young adult CA3-APP mice and age-matched controls.

(C) Quantification of CA3/DG power in different LFP frequency bands. LFP power did not differ between young adult CA3-APP mice and age-matched controls (all p values > 0.05, MW test adjusted for multiple comparisons by Holm-Šídák method).

(D) LFP spectrograms and running speed plots for recording sites in the CA3/DG area of aged mice. Aged CA3-APP mice (n = 8) showed a minor difference in running speed compared with aged control mice (n = 9 mice) in only the choice and reward sub-sections of the maze (Figure S6D). Data are displayed as in (A).

(E) Theta oscillation frequency in the CA3/DG area was lower in aged CA3-APP mice compared with age-matched control mice (p = 0.0029, MW test adjusted for multiple comparisons by Holm-Šídák method). Data are displayed as in (B). Detailed controls for running speed are presented in Figure S6 and Table S9.

(F) CA3/DG LFP power did not differ between aged CA3-APP mice and their control littermates. Data are displayed as in (C). All statistics are reported in Table S13.

and S12). For the frequency of high gamma oscillations, the difference did not reach significance for the CA3/DG recordings (young adult: p = 0.091; aged: p = 0.74, MW tests, Figures 7B and 7E). Power was not altered by CA3-APP expression for any of the frequency bands (Figures 7C, 7F, S11, and S12).

We next asked to what extent the firing properties of CA3/DG cells were altered (Figure S13). Unlike the firing rates in CA1, the firing rates of CA3/DG principal cells remained unchanged in young adult and aged CA3-APP mice compared with age-matched controls (p = 0.058 and 0.96, MW tests), but bursting activity was nonetheless reduced in both age groups (p values < 0.0001, MW tests). Similar to CA1, CA3/DG interneurons did not show differences in their mean firing rate between CA3-APP mice and age-matched controls (young adult: p = 0.65; aged: p = 0.37, MW tests) but had reduced speed modulation in young adult CA3-APP mice (p = 0.0002, MW test). In addition,

normal aging also strongly affected speed modulation of interneurons recorded from the CA3/DG areas, as control-aged mice lacked speed modulation ($p = 0.42$, Wilcoxon signed rank test, Table S15) such that there was no longer a statistical difference between aged control and CA3-APP mice ($p = 0.60$, MW test, Figure S13E). Taken together, the effects of CA3-APP expression on the local network were therefore equal or lesser than on the CA1 network.

Spatial and temporal properties of principal cells and interneurons in the CA3/DG region of CA3-APP mice showed comparable effects to those in the CA1 region

We next evaluated whether place cells in CA3/DG were altered in CA3-APP mice (Figure S14; Table S16). The percentage of place cells in the CA3/DG region of CA3-APP mice was not changed in young adult or aged CA3-APP mice compared with age-matched controls ($p = 0.31$ and 0.70, two-sample t tests, Figures S14C and S14G). Although the peak firing rate of CA3/DG place cells was not altered in CA3-APP mice (young adult: $p = 0.46$; aged: $p = 0.70$, MW tests), the burst index was reduced in both young and aged mice (both p values < 0.0001, MW tests, Figure S14D and S14H). Information content of CA3/DG place cells was already reduced in young adult CA3-APP mice, and the difference to age-matched controls was retained in aged CA3-APP mice ($p = 0.013$ and 0.019, MW tests), while the number of place fields in the maze remained unaltered at both ages ($p = 0.69$ and 0.13, MW tests). Place field size was significantly reduced in CA3/DG cells of young adult CA3-APP mice, but the difference did not reach significance in aged mice ($p = 0.0034$ and 0.75, MW tests). No significant changes were found in trial-by-trial stability or in spatial correlation across sides in CA3-APP mice in both age groups (Figures S14E and S14I). Similar to what we observed in CA1, a large portion of place cells displayed differences in the central arm between left-turn and right-turn trials, and this was not altered in CA3-APP mice compared with age-matched controls (young adult: $p = 0.082$; aged: $p = 0.15$, two-sample t tests, Figures S15A–S15C). The information content and trial-by-trial stability of CA3/DG central-arm cells was not altered in CA3-APP mice of both age groups, although their place field size was larger in young CA3-APP mice but not in aged CA3-APP mice compared with age-matched controls ($p = 0.0007$ and 0.91, MW tests, Figure S15D). In summary, similar to CA1 place cells, there were no consistent patterns in place field changes with CA3-APP expression and, if significant differences were detected, the effect sizes for differences in place cell properties of CA3/DG neurons were small.

Furthermore, we found that changes in the temporal firing properties of CA3/DG cells were quite similar to the ones we report for CA1 cells (see Figure 5). There was already a reduction of the spike oscillation frequency of principal cells in young adult CA3-APP mice ($p < 0.0001$, MW test, Figure 8A), but it was less than the reduction in LFP theta frequency such that the difference between the cells' frequency and the LFP frequency increased ($p = 0.0009$, MW test, Figure S16A). At the younger age, interneurons also showed a small reduction in spike oscillation frequency ($p = 0.016$, MW test, Figure 8C) but without changes in the difference between the cells' and the LFP oscillation frequency ($p = 0.64$, MW test, Figure S16B). No difference was found in the amplitude of theta modulation of principal cells ($p = 0.50$, MW test, Figure 8B) or interneurons ($p = 0.48$, MW test, Figure 8D). In CA3/DG recordings of aged CA3-APP mice we observed a strong reduction in the spike oscillation frequency of both principal cells ($p < 0.0001$, MW test, Figure 8E) and interneurons ($p < 0.0001$, MW test, Figure 8G) and, similar to CA1 recordings, there was a substantial increase in the fraction of cells with oscillations at ~7.5 Hz. The downward shift for principal cell theta oscillation frequency in aged CA3-APP mice was pronounced, such that they were closer in frequency to LFP theta oscillations than in controls ($p < 0.0001$, MW test, Figure S16C), along with a reduced theta modulation amplitude ($p < 0.0001$, MW test, Figure 8F). Interneurons also showed a reduction in the difference to LFP theta oscillation frequency ($p = 0.028$, MW test, Figure S16D) but an increase in theta modulation amplitude (Figure 8H). Strikingly, almost all interneurons in the CA3/DG region had a spike oscillation frequency at ~7.5 Hz (Figure 8G), which was at or below the frequency of LFP theta oscillations.

DISCUSSION

To examine whether the highly localized expression of hAPP alters neuronal activity patterns in cell populations that receive synaptic input from hAPP-expressing neurons but themselves do not harbor hAPP, we performed memory testing and recorded from the hippocampal CA1 region during the memory task in mice that express hAPP in only CA3 principal cells. Despite the restricted pattern of APP expression, hippocampal-dependent memory was partially impaired in young adult CA3-APP mice and substantially impaired in aged CA3-APP mice, indicating that highly localized prolonged hAPP expression can disrupt neural circuit function. In recordings while mice performed the behavioral task, CA1 principal cells of CA3-APP mice exhibited reduced firing rates during behavior, but despite these rate changes, hippocampal spatial coding remained largely intact, even at advanced ages (16–19 months), and the few minor changes that were observed could be a consequence of the reduced firing rates in CA3-APP mice. We rather found a striking number of changes in temporal firing patterns. First, theta and high gamma oscillation frequencies were decreased but without changes in LFP amplitude. Second, subpopulations of principal cells and interneurons showed spike oscillation patterns at lower frequencies than in controls, along with a reduction of theta phase precession of place cells and impaired sequential firing of place cells during the task. Although some of these deficits were already detectable in the CA1 region of young adult CA3-APP mice, the deterioration of temporal coding was more pronounced in aged mice and thus correlated with the progressive worsening of memory deficits. Physiological deficits were therefore pronounced in a brain region that receives synaptic inputs from a cell population that expresses hAPP, but does not locally express hAPP, suggesting that activity-dependent synaptic release of soluble APP fragments, including Aβ,[9] results in network dysfunction. In particular, effects on the temporal and sequential organization of hippocampal patterns were pronounced, even without overt amyloid deposition, cell death, or deficit in place coding. Effects of hAPP on temporal coding are thus a possible cause for early deficits in spatial navigation associated with AD.

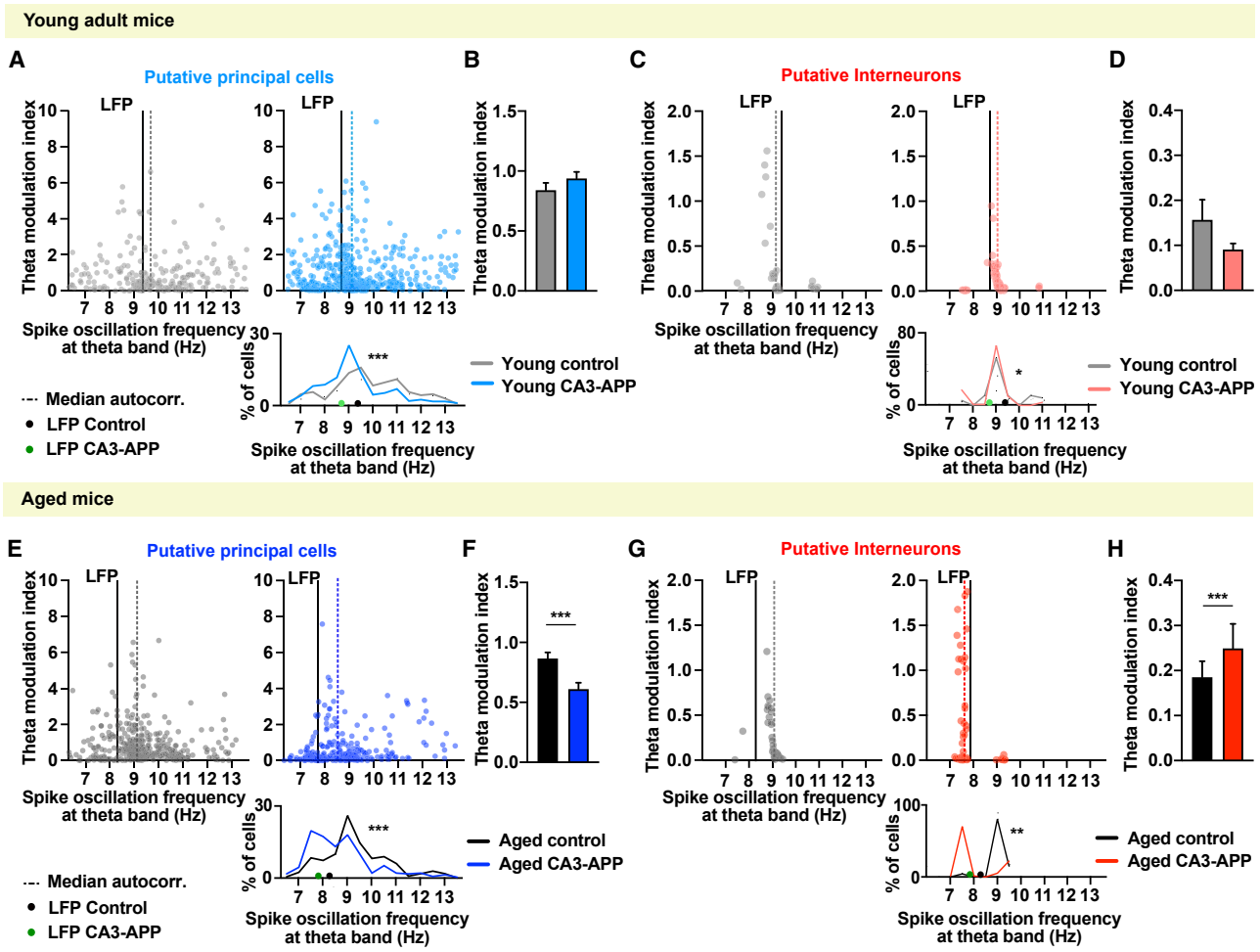

Figure 8. In CA3/DG, spike oscillation frequencies of principal cells in the theta range were reduced to a similar extent as for CA1 principal cells, while frequencies of interneurons in aged CA3-APP mice showed a more pronounced effect

(A) Spike oscillation frequencies of CA3/DG principal cells are plotted as in Figure 5A and were lower in young adult CA3-APP mice compared with age-matched controls (n = 500 and 226 cells for CA3-APP mice and controls, $p < 0.0001$, MW test).

(B) Average theta modulation amplitude (theta modulation index) of all active CA3/DG principal cells did not differ between cells from young adult CA3-APP mice and age-matched controls (n = 566 and 297 cells, $p = 0.50$, MW test).

(C) In young adult CA3 APP mice, there was a minor reduction in the spike oscillation frequency of CA3/DG interneurons compared with age-matched controls (n = 87 and 36 cells, $p = 0.016$, MW test). Data are displayed as in (A).

(D) Average theta modulation index of CA3/DG interneurons. Theta modulation amplitude of interneurons did not differ between young adult CA3-APP mice and age-matched controls (n = 111 and 59 cells, $p = 0.48$, MW test).

(E) When compared with age-matched controls, principal cells from aged CA3-APP mice showed a major reduction in the spike oscillation frequency, with a large fraction of cells oscillating between 7 and 8 Hz (n = 289 and 380 cells in CA3-APP mice and controls, $p < 0.0001$, MW test). Data are displayed as in (A).

(F) Theta modulation amplitude of CA3/DG principal cells of CA3-APP mice was reduced compared with cells from age-matched controls (n = 316 and 425 cells, $p < 0.0001$, MW test).

(G) Compared with age-matched controls, CA3/DG interneurons from aged CA3-APP mice showed a pronounced reduction in spike oscillation frequencies, with almost all interneurons now oscillating below 8 Hz (n = 106 and 52 cells in CA3-APP mice and controls, $p < 0.0001$, MW test). Data are displayed as in (A).

(H) Interneurons from aged CA3-APP mice showed an increase in theta modulation amplitude compared with age-matched control mice (n = 106 and 52 cells, $p < 0.0001$, MW test).

Bar graphs with error bars correspond to the mean ± SEM. Data and statistics are reported in Table S17.

The predominant effect on temporal firing rather than on spatial properties of CA1 cells differs from previous studies in pan-neuronal models of amyloidosis that have linked impaired spatial properties of spatially modulated cells, such as place[15,20,37] and grid cells[16,22] with memory deficits. However, the majority of previous recordings were performed at advanced stages of amyloid pathology, when plaques, robust spine loss, and sometimes cell death were already present. Similarly, major effects on place cells and grid cells were also observed in tau models, again at stages with substantial neurodegeneration,[18,38] which makes it challenging to infer whether memory deficits and spatial coding deficits arise as a direct effect of the primary

pathology or more indirectly from loss of synapses and neurons. Together with findings that deficits in spatial memory in AD arise in early disease stages, a severely degraded hippocampal place code might not be directly correlated with behavior impairment. Even in healthy mice, the extent of spatial coding deficits is not a good predictor for memory deficits, as shown in studies in which hippocampal-dependent memory deficits occur while the place code in CA1 is intact.[39,40] It has therefore been suggested that the generation of distinct hippocampal maps across different environments may be a better indicator for memory dysfunction in disease models.[16] Although this may be relevant for memory tasks that require discrimination between spatial contexts, previous recordings were not performed in a discrimination task. In contrast, we performed our recordings in a hippocampus-dependent memory task, and the task included a stem section where differences in firing patterns could directly relate to past or future turn direction.[41] When restricting our analysis to the stem, the firing patterns of CA1 cells were as distinct between turn directions in CA3-APP mice as in control mice, which makes it unlikely that less distinct coding in the stem was the cause of memory deficits.

Because we did not observe substantial deficits in spatial coding in CA1, which does itself not express hAPP, we also examined the possibility that the pronounced coding deficits that have previously been reported in AD models with pan-neuronal APP expression may require local hAPP expression. We therefore examined whether we could detect more severe deficits in circuit function in the CA3 region, which does not only receive inputs from APP-expressing cells via its recurrent collaterals but also locally expresses hAPP. Firing patterns in the CA3/DG region of CA3-APP mice were generally very similar to those in the CA1 region. Some effects, such as those on high gamma oscillation frequency, were less pronounced in the CA3/DG region than in CA1, but this could be a consequence of greater prominence of high gamma oscillations in CA1 compared with CA3.[42] Together, these findings suggest that local hAPP expression does not further exacerbate the deterioration of the cells' firing patterns and that, in turn, synaptic inputs from hAPP-expressing cells are sufficient to result in circuit dysfunction.[9] For the effects on CA3 cells, we cannot exclude the possibility that local release of Aβ from the soma and dendrites, as has been reported in tissue culture with high APP expression levels,[10,43] also contributes to circuit dysfunction. However, in the intact brain, soluble Aβ is released from presynaptic terminals, presynaptic APP expression is sufficient for LTP impairment and spine loss, and amyloid plaques preferentially accumulate at the synaptic termination site of APP-expressing cells.[9,25,44] Together with studies that have compellingly shown that soluble forms of Aβ acutely result in functional synaptic deficits,[11] our results therefore suggest that APP expression in presynaptic neurons, which leads to release of soluble APP fragments from presynaptic terminals,[9] is sufficient to result in the emergence of aberrant temporal firing patterns in postsynaptic non-expressing cells. Once temporal firing patterns begin to be disrupted, the mistimed firing could by itself contribute to further circuit dysfunction or, alternatively, the sustained release of soluble APP fragments over many months could result in further synaptic and circuit dysfunction.

Furthermore, our finding that APP expression in synaptic inputs is sufficient to result in altered neuronal firing patterns, such as lower CA1 firing rates, is consistent with the finding that dentate granule (DG) cells show lower levels of immediate-early gene expression when their input neurons, but not DG cells themselves, express APP.[45] However, in many hours of recordings from each CA3-APP mouse, there was no evidence of the emergence of epileptiform activity, as has been described with APP expression in the entorhinal cortex. A major difference between our CA3-APP model and the EC-APP model is that the latter is only partially regionally restricted. In EC-APP mice, the APP expression is also observed in cortical areas other than EC, and plaques are deposited at the site where epileptiform activity emerges.[8,45] We also did not observe the hyperactivity that has been reported in response to acute Aβ and before plaque deposition in the APPPS1 model[8] and rather report moderately decreased firing rates and bursting. Given that we show major differences in interneuron firing patterns, but with APP expression in only excitatory neurons, it is feasible that changes at synapses from excitatory neurons to inhibitory neurons compensate and reset the excitation-inhibition balance in parallel with the emergence of mistimed firing patterns.

Although many firing properties show a comparable or lesser effect in CA3/DG than in CA1, one effect that is more pronounced in the CA3/DG cell population is the decrease in the spike oscillation frequency of interneurons. According to anatomical studies, the interneurons in this region are mostly composed of basket cells (cholecystokinin or parvalbumin positive) and bistratified cells (somatostatin and parvalbumin positive),[46] and all of these receive projections from CA3 principal cells, which express hAPP in the CA3-APP mice. However, in the CA3-APP mouse, the CA3/DG interneurons themselves do not directly express APP (Figure S1B). Our study is therefore the first to evaluate interneuron physiology in the context of AD without directly expressing AD-related proteins in interneurons.[47–49] The fact that a large fraction of interneurons in CA3-APP mice show major temporal reorganization, such as large shifts in oscillation frequency and lack of speed modulation, points to the importance of considering interneurons as major hubs for the manifestation of disease pathology. Although a previous study pointed to the role of sodium channels that could be altered by either cellular or presynaptic APP expression,[49] our results highlight the importance of investigating how synapses between APP-expressing afferent neurons and interneurons are altered in the context of AD.[50–52] In particular, we also find that a subset of principal neurons shows a decrease in spike oscillation frequency that corresponds to the shift in the frequency that is observed for interneurons. This suggests that feedback loops between excitatory and inhibitory cells could amplify the pathology but with APP expression in principal neurons that are presynaptic to interneurons driving the changes.

As a consequence of the changes in oscillations and feedback loops in networks that include interneurons and principal cells, CA3-APP mice show a large reduction in theta frequency and in the associated high gamma oscillations that are thought to emerge locally.[53] Recent studies have also described a reduction in theta frequency in pan-neuronal models of AD and that optogenetic stimulation at theta frequency has the potential to ameliorate hippocampal memory in these mice (J20 and APP/PS1).[47,54] Our work adds to these studies by showing that a reduction in theta

oscillation frequency can already emerge from a restricted pathology, which does not have to directly include interneurons. Our finding, that effects on oscillations appear prior to other physiological changes and are present along with behavioral deficits, provides further support for using the strategy of theta pacing to rescue memory function. Furthermore, the more pronounced spatial navigation deficits in aged compared with young adult CA3-APP mice were accompanied by an impairment in sequential firing within theta cycles and by a reduction in phase precession in the version of the memory task that is hippocampus dependent (i.e., with 2-s and 10-s delay).

Although our findings of a disrupted temporal organization of hippocampal firing patterns might appear to be at odds with a previous report from a Tau AD model, where place cells were largely impaired but the sequential activity of cells was maintained,[18] it is important to note that the Tau model is characterized by a loss of more than 50% of neurons in the CA1 pyramidal layer at the time of recordings. Therefore, the rigid firing sequences might represent an advanced disease stage, when compensatory mechanisms maintain highly stereotyped sequential firing of hippocampal cells. In contrast, our model would resemble early pathology, when hippocampal firing becomes progressively disorganized and can no longer support computations for spatial memory and navigation, which is characteristic for early AD patients. In particular, the restricted expression of hAPP in only one hippocampal subregion shows that early effects on circuits are primarily on the temporal organization of firing patterns and that interneurons are important in mediating these effects. During disease progression, other circuit elements are therefore not only affected by spreading molecular pathology but also by dysfunction that emerges in networks that are postsynaptic to the primary pathology, such as observed here for the firing properties of interneurons and CA1 cells.

STAR★METHODS

Detailed methods are provided in the online version of this paper and include the following:

- KEY RESOURCES TABLE
- RESOURCE AVAILABILITY
  - Lead contact
  - Materials availability
  - Data and code availability
- EXPERIMENTAL MODEL AND STUDY PARTICIPANT DETAILS
- METHOD DETAILS
  - Behavior equipment
  - Behavior training and testing
  - Electrode implant surgery
  - Electrophysiology recordings
  - Histology and tetrode locations
  - Immunohistochemistry
  - Spike sorting and cluster quality
  - Unit classification
  - LFP analysis
  - Firing properties of single units
  - Place cell analysis
  - Place cell spatial correlations
  - Temporal properties of single units
  - Phase precession and sequence compression
- QUANTIFICATION AND STATISTICAL ANALYSIS

SUPPLEMENTAL INFORMATION

Supplemental information can be found online at https://doi.org/10.1016/j.neuron.2023.10.001.

ACKNOWLEDGMENTS

We would like to thank Dr. Marta Sabariego for discussions and behavioral protocol design and Dr. Ipshita Zutshi for invaluable discussions and analysis scripts. We also thank Dr. Brittney Boublil, Gecelle DeGuia, Tiffany Huynh, and Ellen Lee for technical assistance. This work was funded by NIH grants R01 NS084324, R01 NS102915, and R01 NS097772 to S.L., R01 MH119179 to J.K.L., and Deutsche Forschungsgemeinschaft grant EXC-2049-390688087 to S.V.d.S.

AUTHOR CONTRIBUTIONS

S.V.d.S., K.G., R.P., G.N., M.L., M.L.F., and M.d.C.V. conducted the experiments; S.V.d.S. and M.G.H. performed the analysis; S.V.d.S., E.H.K., J.K.L., and S.L. designed the experiments and S.V.d.S., J.K.L., and S.L. wrote the paper.

DECLARATION OF INTERESTS

The authors declare no competing interests.

Received: December 26, 2022
Revised: June 16, 2023
Accepted: October 2, 2023
Published: October 30, 2023

REFERENCES

1. Coughlan, G., Laczó, J., Hort, J., Minihane, A.M., and Hornberger, M. (2018). Spatial navigation deficits - overlooked cognitive marker for preclinical Alzheimer disease? Nat. Rev. Neurol. *14*, 496–506. https://doi.org/10.1038/s41582-018-0031-x.
2. Mapstone, M., Steffenella, T.M., and Duffy, C.J. (2003). A visuospatial variant of mild cognitive impairment: getting lost between aging and AD. Neurology *60*, 802–808. https://doi.org/10.1212/01.wnl.0000049471.76799.de.
3. Buzsáki, G., and Moser, E.I. (2013). Memory, navigation and theta rhythm in the hippocampal-entorhinal system. Nat. Neurosci. *16*, 130–138. https://doi.org/10.1038/nn.3304.
4. Palop, J.J., and Mucke, L. (2016). Network abnormalities and interneuron dysfunction in Alzheimer disease. Nat. Rev. Neurosci. *17*, 777–792. https://doi.org/10.1038/nrn.2016.141.
5. Mucke, L., Masliah, E., Yu, G.Q., Mallory, M., Rockenstein, E.M., Tatsuno, G., Hu, K., Kholodenko, D., Johnson-Wood, K., and McConlogue, L. (2000). High-level neuronal expression of abeta 1–42 in wild-type human amyloid protein precursor transgenic mice: synaptotoxicity without plaque formation. J. Neurosci. *20*, 4050–4058. https://doi.org/10.1523/JNEUROSCI.20-11-04050.2000.
6. Hsia, A.Y., Masliah, E., McConlogue, L., Yu, G.Q., Tatsuno, G., Hu, K., Kholodenko, D., Malenka, R.C., Nicoll, R.A., and Mucke, L. (1999). Plaque-independent disruption of neural circuits in Alzheimer's disease mouse models. Proc. Natl. Acad. Sci. USA *96*, 3228–3233. https://doi.org/10.1073/pnas.96.6.3228.
7. Jacobsen, J.S., Wu, C.C., Redwine, J.M., Comery, T.A., Arias, R., Bowlby, M., Martone, R., Morrison, J.H., Pangalos, M.N., Reinhart, P.H., et al.

(2006). Early-onset behavioral and synaptic deficits in a mouse model of Alzheimer's disease. Proc. Natl. Acad. Sci. USA *103*, 5161–5166. https://doi.org/10.1073/pnas.0600948103.

8. Busche, M.A., Chen, X., Henning, H.A., Reichwald, J., Staufenbiel, M., Sakmann, B., and Konnerth, A. (2012). Critical role of soluble amyloid-β for early hippocampal hyperactivity in a mouse model of Alzheimer's disease. Proc. Natl. Acad. Sci. USA *109*, 8740–8745. https://doi.org/10.1073/pnas.1206171109.
9. Cirrito, J.R., Yamada, K.A., Finn, M.B., Sloviter, R.S., Bales, K.R., May, P.C., Schoepp, D.D., Paul, S.M., Mennerick, S., and Holtzman, D.M. (2005). Synaptic activity regulates interstitial fluid amyloid-beta levels in vivo. Neuron *48*, 913–922. https://doi.org/10.1016/j.neuron.2005.10.028.
10. Kamenetz, F., Tomita, T., Hsieh, H., Seabrook, G., Borchelt, D., Iwatsubo, T., Sisodia, S., and Malinow, R. (2003). APP processing and synaptic function. Neuron *37*, 925–937. https://doi.org/10.1016/s0896-6273(03)00124-7.
11. Selkoe, D.J. (2008). Soluble oligomers of the amyloid β-protein impair synaptic plasticity and behavior. Behav. Brain Res. *192*, 106–113. https://doi.org/10.1016/j.bbr.2008.02.016.
12. Busche, M.A., Kekuš, M., Adelsberger, H., Noda, T., Förstl, H., Nelken, I., and Konnerth, A. (2015). Rescue of long-range circuit dysfunction in Alzheimer's disease models. Nat. Neurosci. *18*, 1623–1630. https://doi.org/10.1038/nn.4137.
13. Grienberger, C., Rochefort, N.L., Adelsberger, H., Henning, H.A., Hill, D.N., Reichwald, J., Staufenbiel, M., and Konnerth, A. (2012). Staged decline of neuronal function in vivo in an animal model of Alzheimer's disease. Nat. Commun. *3*, 774. https://doi.org/10.1038/ncomms1783.
14. Prince, S.M., Paulson, A.L., Jeong, N., Zhang, L., Amigues, S., and Singer, A.C. (2021). Alzheimer's pathology causes impaired inhibitory connections and reactivation of spatial codes during spatial navigation. Cell Rep. *35*, 109008. https://doi.org/10.1016/j.celrep.2021.109008.
15. Mably, A.J., Gereke, B.J., Jones, D.T., and Colgin, L.L. (2017). Impairments in spatial representations and rhythmic coordination of place cells in the 3xTg mouse model of Alzheimer's disease. Hippocampus *27*, 378–392. https://doi.org/10.1002/hipo.22697.
16. Jun, H., Bramian, A., Soma, S., Saito, T., Saido, T.C., and Igarashi, K.M. (2020). Disrupted place cell remapping and impaired grid cells in a Knockin model of Alzheimer's disease. Neuron *107*, 1095–1112.e6. https://doi.org/10.1016/j.neuron.2020.06.023.
17. Poll, S., Mittag, M., Musacchio, F., Justus, L.C., Giovannetti, E.A., Steffen, J., Wagner, J., Zohren, L., Schoch, S., Schmidt, B., et al. (2020). Memory trace interference impairs recall in a mouse model of Alzheimer's disease. Nat. Neurosci. *23*, 952–958. https://doi.org/10.1038/s41593-020-0652-4.
18. Cheng, J., and Ji, D. (2013). Rigid firing sequences undermine spatial memory codes in a neurodegenerative mouse model. eLife *2*, e00647. https://doi.org/10.7554/eLife.00647.
19. Ciupek, S.M., Cheng, J., Ali, Y.O., Lu, H.C., and Ji, D. (2015). Progressive functional impairments of hippocampal neurons in a tauopathy mouse model. J. Neurosci. *35*, 8118–8131. https://doi.org/10.1523/JNEUROSCI.3130-14.2015.
20. Cacucci, F., Yi, M., Wills, T.J., Chapman, P., and O'Keefe, J. (2008). Place cell firing correlates with memory deficits and amyloid plaque burden in Tg2576 Alzheimer mouse model. Proc. Natl. Acad. Sci. USA *105*, 7863–7868. https://doi.org/10.1073/pnas.0802908105.
21. Fu, H., Rodriguez, G.A., Herman, M., Emrani, S., Nahmani, E., Barrett, G., Figueroa, H.Y., Goldberg, E., Hussaini, S.A., and Duff, K.E. (2017). Tau pathology induces excitatory neuron loss, grid cell dysfunction, and spatial memory deficits reminiscent of early Alzheimer's disease. Neuron *93*, 533–541.e5. https://doi.org/10.1016/j.neuron.2016.12.023.
22. Ying, J., Keinath, A.T., Lavoie, R., Vigneault, E., El Mestikawy, S., and Brandon, M.P. (2022). Disruption of the grid cell network in a mouse model of early Alzheimer's disease. Nat. Commun. *13*, 886. https://doi.org/10.1038/s41467-022-28551-x.
23. Sasaguri, H., Nilsson, P., Hashimoto, S., Nagata, K., Saito, T., De Strooper, B., Hardy, J., Vassar, R., Winblad, B., and Saido, T.C. (2017). APP mouse models for Alzheimer's disease preclinical studies. EMBO J. *36*, 2473–2487. https://doi.org/10.15252/embj.201797397.
24. de Calignon, A., Polydoro, M., Suárez-Calvet, M., William, C., Adamowicz, D.H., Kopeikina, K.J., Pitstick, R., Sahara, N., Ashe, K.H., Carlson, G.A., et al. (2012). Propagation of tau pathology in a model of early Alzheimer's disease. Neuron *73*, 685–697. https://doi.org/10.1016/j.neuron.2011.11.033.
25. Vicario-Orri, E., Kasuga, K., Tyan, S.-H., Chiang, K., da Silva, S.V., Bushong, E.A., DeLoach, K., Ling, I.-F., Luo, L., Ellisman, M.H., et al. (2020). Aβ-induced synaptic injury is mediated by presynaptic expression of amyloid precursor protein (APP) in hippocampal neurons. bioRxiv *955*. 07.18.210344. https://doi.org/10.1101/2020.07.18.210344.
26. Ainge, J.A., Tamosiunaite, M., Woergoetter, F., and Dudchenko, P.A. (2007). Hippocampal CA1 place cells encode intended destination on a maze with multiple choice points. J. Neurosci. *27*, 9769–9779. https://doi.org/10.1523/JNEUROSCI.2011-07.2007.
27. Heneka, M.T., Carson, M.J., El Khoury, J.E., Landreth, G.E., Brosseron, F., Feinstein, D.L., Jacobs, A.H., Wyss-Coray, T., Vitorica, J., Ransohoff, R.M., et al. (2015). Neuroinflammation in Alzheimer's disease. Lancet Neurol. *14*, 388–405. https://doi.org/10.1016/S1474-4422(15)70016-5.
28. Kropff, E., Carmichael, J.E., Moser, M.B., and Moser, E.I. (2015). Speed cells in the medial entorhinal cortex. Nature *523*, 419–424. https://doi.org/10.1038/nature14622.
29. Sabariego, M., Schönwald, A., Boublil, B.L., Zimmerman, D.T., Ahmadi, S., Gonzalez, N., Leibold, C., Clark, R.E., Leutgeb, J.K., and Leutgeb, S. (2019). Time cells in the hippocampus are neither dependent on medial entorhinal cortex inputs nor necessary for spatial working memory. Neuron *102*, 1235–1248.e5. https://doi.org/10.1016/j.neuron.2019.04.005.
30. Singer, A.C., Karlsson, M.P., Nathe, A.R., Carr, M.F., and Frank, L.M. (2010). Experience-dependent development of coordinated hippocampal spatial activity representing the similarity of related locations. J. Neurosci. *30*, 11586–11604. https://doi.org/10.1523/JNEUROSCI.0926-10.2010.
31. Colgin, L.L. (2016). Rhythms of the hippocampal network. Nat. Rev. Neurosci. *17*, 239–249. https://doi.org/10.1038/nrn.2016.21.
32. Buzsáki, G., Anastassiou, C.A., and Koch, C. (2012). The origin of extracellular fields and currents — EEG, ECoG, LFP and spikes. Nat. Rev. Neurosci. *13*, 407–420. https://doi.org/10.1038/nrn3241.
33. Einevoll, G.T., Kayser, C., Logothetis, N.K., and Panzeri, S. (2013). Modelling and analysis of local field potentials for studying the function of cortical circuits. Nat. Rev. Neurosci. *14*, 770–785. https://doi.org/10.1038/nrn3599.
34. O'Keefe, J., and Recce, M.L. (1993). Phase relationship between hippocampal place units and the EEG theta rhythm. Hippocampus *3*, 317–330. https://doi.org/10.1002/hipo.450030307.
35. Skaggs, W.E., McNaughton, B.L., Wilson, M.A., and Barnes, C.A. (1996). Theta phase precession in hippocampal neuronal populations and the compression of temporal sequences. Hippocampus *6*, 149–172. https://doi.org/10.1002/(SICI)1098-1063(1996)6:2<149::AID-HIPO6>3.0.CO;2-K.
36. Dragoi, G., and Buzsáki, G. (2006). Temporal encoding of place sequences by hippocampal cell assemblies. Neuron *50*, 145–157. https://doi.org/10.1016/j.neuron.2006.02.023.
37. Rechnitz, O., Slutsky, I., Morris, G., and Derdikman, D. (2021). Hippocampal sub-networks exhibit distinct spatial representation deficits in Alzheimer's disease model mice. Curr. Biol. *31*, 3292–3302.e6. https://doi.org/10.1016/j.cub.2021.05.039.
38. Ridler, T., Witton, J., Phillips, K.G., Randall, A.D., and Brown, J.T. (2020). Impaired speed encoding and grid cell periodicity in a mouse model of tauopathy. eLife *9*. https://doi.org/10.7554/eLife.59045.
39. Munn, R.G.K., Freeburn, A., Finn, D.P., and Heller, H.C. (2022). Hyper-rigid phasic organization of hippocampal activity but normal spatial properties of CA1 place cells in the Ts65Dn mouse model of Down syndrome.

J. Neurosci. *42*, 1542–1556. https://doi.org/10.1523/JNEUROSCI.2636-20.2021.

40. Talbot, Z.N., Sparks, F.T., Dvorak, D., Curran, B.M., Alarcon, J.M., and Fenton, A.A. (2018). Normal CA1 place fields but discoordinated network discharge in a Fmr1-null mouse model of fragile X syndrome. Neuron *97*, 684–697.e4. https://doi.org/10.1016/j.neuron.2017.12.043.
41. Duvelle, É., Grieves, R.M., and van der Meer, M.A.A. (2023). Temporal context and latent state inference in the hippocampal splitter signal. eLife *12*, e82357. https://doi.org/10.7554/eLife.82357.
42. Colgin, L.L., Denninger, T., Fyhn, M., Hafting, T., Bonnevie, T., Jensen, O., Moser, M.B., and Moser, E.I. (2009). Frequency of gamma oscillations routes flow of information in the hippocampus. Nature *462*, 353–357. https://doi.org/10.1038/nature08573.
43. Wei, W., Nguyen, L.N., Kessels, H.W., Hagiwara, H., Sisodia, S., and Malinow, R. (2010). Amyloid beta from axons and dendrites reduces local spine number and plasticity. Nat. Neurosci. *13*, 190–196. https://doi.org/10.1038/nn.2476.
44. Yamamoto, K., Tanei, Z.I., Hashimoto, T., Wakabayashi, T., Okuno, H., Naka, Y., Yizhar, O., Fenno, L.E., Fukayama, M., Bito, H., et al. (2015). Chronic optogenetic activation augments aβ pathology in a mouse model of Alzheimer disease. Cell Rep. *11*, 859–865. https://doi.org/10.1016/j.celrep.2015.04.017.
45. Harris, J.A., Devidze, N., Verret, L., Ho, K., Halabisky, B., Thwin, M.T., Kim, D., Hamto, P., Lo, I., Yu, G.Q., et al. (2010). Transsynaptic progression of amyloid-β-induced neuronal dysfunction within the entorhinal-hippocampal network. Neuron *68*, 428–441. https://doi.org/10.1016/j.neuron.2010.10.020.
46. Topolnik, L., and Tamboli, S. (2022). The role of inhibitory circuits in hippocampal memory processing. Nat. Rev. Neurosci. *23*, 476–492. https://doi.org/10.1038/s41583-022-00599-0.
47. Etter, G., van der Veldt, S., Manseau, F., Zarrinkoub, I., Trillaud-Doppia, E., and Williams, S. (2019). Optogenetic gamma stimulation rescues memory impairments in an Alzheimer's disease mouse model. Nat. Commun. *10*, 5322. https://doi.org/10.1038/s41467-019-13260-9.
48. Gillespie, A.K., Jones, E.A., Lin, Y.H., Karlsson, M.P., Kay, K., Yoon, S.Y., Tong, L.M., Nova, P., Carr, J.S., Frank, L.M., et al. (2016). Apolipoprotein E4 causes age-dependent disruption of slow gamma oscillations during hippocampal sharp-wave ripples. Neuron *90*, 740–751. https://doi.org/10.1016/j.neuron.2016.04.009.
49. Verret, L., Mann, E.O., Hang, G.B., Barth, A.M.I., Cobos, I., Ho, K., Devidze, N., Masliah, E., Kreitzer, A.C., Mody, I., et al. (2012). Inhibitory interneuron deficit links altered network activity and cognitive dysfunction in Alzheimer model. Cell *149*, 708–721. https://doi.org/10.1016/j.cell.2012.02.046.
50. Hijazi, S., Heistek, T.S., Scheltens, P., Neumann, U., Shimshek, D.R., Mansvelder, H.D., Smit, A.B., and van Kesteren, R.E. (2020). Early restoration of parvalbumin interneuron activity prevents memory loss and network hyperexcitability in a mouse model of Alzheimer's disease. Mol. Psychiatry *25*, 3380–3398. https://doi.org/10.1038/s41380-019-0483-4.
51. Schmid, L.C., Mittag, M., Poll, S., Steffen, J., Wagner, J., Geis, H.R., Schwarz, I., Schmidt, B., Schwarz, M.K., Remy, S., et al. (2016). Dysfunction of somatostatin-positive interneurons associated with memory deficits in an Alzheimer's disease model. Neuron *92*, 114–125. https://doi.org/10.1016/j.neuron.2016.08.034.
52. Viana da Silva, S., Zhang, P., Haberl, M.G., Labrousse, V., Grosjean, N., Blanchet, C., Frick, A., and Mulle, C. (2019). Hippocampal mossy fibers synapses in CA3 pyramidal cells are altered at an early stage in a mouse model of Alzheimer's disease. J. Neurosci. *39*, 4193–4205. https://doi.org/10.1523/JNEUROSCI.2868-18.2019.
53. Lasztóczi, B., and Klausberger, T. (2016). Hippocampal place cells couple to three different gamma oscillations during place field traversal. Neuron *91*, 34–40. https://doi.org/10.1016/j.neuron.2016.05.036.
54. Giovannetti, E.A., Poll, S., Justus, D., Kaneko, H., Fuhrmann, F., Steffen, J., Remy, S., and Fuhrmann, M. (2018). Restoring memory by optogenetic synchronization of hippocampal oscillations in an Alzheimer's disease mouse model. bioRxiv, 363820. https://doi.org/10.1101/363820.
55. Li, L., Tasic, B., Micheva, K.D., Ivanov, V.M., Spletter, M.L., Smith, S.J., and Luo, L. (2010). Visualizing the distribution of synapses from individual neurons in the mouse brain. PLOS One *5*, e11503. https://doi.org/10.1371/journal.pone.0011503.
56. Jankowsky, J.L., Slunt, H.H., Gonzales, V., Savonenko, A.V., Wen, J.C., Jenkins, N.A., Copeland, N.G., Younkin, L.H., Lester, H.A., Younkin, S.G., et al. (2005). Persistent amyloidosis following suppression of Abeta production in a transgenic model of Alzheimer disease. PLOS Med. *2*, e355. https://doi.org/10.1371/journal.pmed.0020355.
57. Nakazawa, K.K., Quirk, M.C.M., Chitwood, R.A.R., Watanabe, M.M., Yeckel, M.F.M., Sun, L.D.L., Kato, A.A., Carr, C.A.C., Johnston, D.D., Wilson, M.A.M., et al. (2002). Requirement for hippocampal CA3 NMDA receptors in associative memory recall. Science *297*, 211–218. https://doi.org/10.1126/science.1071795.
58. Anikeeva, P., Andalman, A.S., Witten, I., Warden, M., Goshen, I., Grosenick, L., Gunaydin, L.A., Frank, L.M., and Deisseroth, K. (2011). Optetrode: a multichannel readout for optogenetic control in freely moving mice. Nat. Neurosci. *15*, 163–170. https://doi.org/10.1038/nn.2992.
59. Schmitzer-Torbert, N., Jackson, J., Henze, D., Harris, K., and Redish, A.D. (2005). Quantitative measures of cluster quality for use in extracellular recordings. SfN. Neuroscience *131*, 1–11. 131. https://doi.org/10.1016/j.neuroscience.2004.09.066.
60. Torrence, C., and Compo, G.P. (1998). A practical guide to wavelet analysis. Bull. Amer. Meteor. Soc. *79*, 61–78. https://doi.org/10.1175/1520-0477(1998)079<0061:APGTWA>2.0.CO;2.
61. Royer, S., Zemelman, B.V., Losonczy, A., Kim, J., Chance, F., Magee, J.C., and Buzsáki, G. (2012). Control of timing, rate and bursts of hippocampal place cells by dendritic and somatic inhibition. Nat. Neurosci. *15*, 769–775. https://doi.org/10.1038/nn.3077.

STAR★METHODS

KEY RESOURCES TABLE

REAGENT or RESOURCE	SOURCE	IDENTIFIER
Antibodies		
Mouse IgG1 Biotin anti-β-Amyloid, 1-16 Antibody (6E10 clone)	Covance/BioLegend	RRID: AB_2564658 BioLegend Cat# 803008
Rabbit Anit-GAD67 Polyclonal Antibody	Invitrogen	RRID: AB_11153284 Cat# PA5-21397
Chicken Anti NeuN Polyclonal Antibody	Sigma-Aldrich	RRID: AB_11205760 Cat# ABN91
Alexa Fluor™ 488 Tyramide SuperBoost™ Kit, streptavidin	Thermofisher Scientific	Cat# B40932
Experimental models: Organisms/strains		
ROSA26-ZtTA	S. Tonegawa	RRID: IMSR_JAX:012266
tetO-APPswe/ind	J. L. Jankowsky	RRID: MMRRC_034845-JAX
C57BL/6-Tg(Grik4-cre) G32-4Stl/J	S. Tonegawa	RRID: IMSR_JAX:006474
Crl:CD1(ICR)	Charles River	RRID: IMSR_CRL:022
Software and algorithms		
MATLAB	Mathworks	RRID:SCR_001622
MClust	A.D. Redish	https://github.com/adredish/MClust-Spike-Sorting-Toolbox
Custom code for data processing	Viana da Silva et al.	https://github.com/SilviaVianaSilva/VianadaSilva_Neuron2023
Other		
Platinum-iridium tetrode wire	California fine wire company	Cat #: CFW0011873
Digital neuralynx recording system	Neuralynx	Model: Digital Lynx SX

RESOURCE AVAILABILITY

Lead contact

Further information and requests for resources and reagents should be directed to and will be fulfilled by the lead contact, Stefan Leutgeb (sleutgeb@ucsd.edu).

Materials availability

This study did not generate new unique reagents.

Data and code availability

- All the data reported in this paper will be shared by the lead contact upon request (sleutgeb@ucsd.edu).
- All custom code for processing the data is freely available from a GitHub repository (https://github.com/SilviaVianaSilva/VianadaSilva_Neuron2023).
- Any additional information required to reanalyze the data reported in this paper is available from the lead contact upon request.

EXPERIMENTAL MODEL AND STUDY PARTICIPANT DETAILS

All experimental procedures were conducted at the University of California, San Diego according to National Institutes of Health guidelines and were approved by the Institutional Animal Care and Use Committee. The targeting of hAPP was achieved by crossing three transgenic mouse lines (Figure 1A), as previously described.[25] In brief, ROSA26-ZtTA transgenic mice (JAX Stock No: 012266)[55] were first crossed with tetO-APPswe/ind transgenic mice (MMRRC Stock No: 34846-JAX)[56] and the resulting ZtTA/tet-APP bi-transgenic mice were then crossed with Grik4-cre mice (JAX Stock No: 006474).[57] The Grik4-Cre[57] transgene provided the selectivity for CA3 principal cells, while the combination of Cre-dependent tTA[55] and tetO-APP transgenes[56] allowed for cell-type specific

expression of hAPP carrying the Swedish and Indiana mutations (Figure 1B). Triple transgenic male breeders were crossed to CD-1 female mice to obtain the experimental mice with mixed strain backgrounds (C57Bl6/J and CD-1). This crossing strategy ensured large litters, which were necessary to obtain the needed number of triple transgenic CA3-APP mice. We used offspring that was positive for the three transgenes as CA3-APP mice, and littermates that did not carry the tetO-APP transgene as controls to account for possible leakage of the promoter (see Table S1 for more details). The number of animals analyzed is reported in each figure and summarized in Table S1, along with their sex and exact genotype. Mice were kept on a 12-hour light-dark cycle (light on from 7AM to 7PM), and all the experimental data was recorded in the light phase to improve the likelihood that mice were quiet during the rest sessions before and after behavior testing. All mice were group housed (maximum 5 per cage) with food and water *ad libitum* until the beginning of behavioral training at 4 or 16 months, and from then, were single housed and food restricted.

METHOD DETAILS

Behavior equipment

Mice were trained on a figure-8 shaped maze (Figure 1C) 50 cm by 75 cm long. The maze runways were made of dark grey Plexiglas 5 cm wide with a 0.5 cm high border. The figure-8 maze was elevated 55 cm above the floor and positioned in the center of a room where a bench, an acquisition system and a dim light source served as prominent visual cues. Two barriers made of vinyl-covered cardboard were used to confine the animals in the initial 20 cm of the central runway (delay area, Figure 3A). Sugar pellets were attached below the runaways at the reward sites to provide permanent odor cues. During the rest periods mice were in their home cage inside a tall transparent Plexiglas box that was placed on the bench, 1.2 m from the floor.

Behavior training and testing

One week before the start of behavioral training transgenic mice and littermate controls were single housed and food restricted to 85-90% of their baseline body weight. Nesting materials and light enrichment was provided. Mice were handled for 5-10 minutes a day during a *habituation phase*, when they were also allowed to forage for sugar pellets (20 mg; Test Diet) scattered in the figure-8 maze. Once mice consistently ate the scattered sugar pellets, behavior training was initiated. First, mice were guided and trained to run in one direction and to alternate between left and right turns to find reward at the end of the right and left arms (i.e., in the reward area). The experimenter was always on the side where the rewards were located to refill. Mice ran one session of 20 minutes a day, and after 2 consecutive days of consistently eating the reward pellets and running without turning back, mice advanced to the next phase of behavior training during which all barriers and guidance were removed. During this phase mice ran 20 minutes or 60 laps receiving a reward only for correct (alternating) turns. Once the criterium of >80% correct turns for 4 out of 5 consecutive days was reached, mice advanced to the testing phase, when a delay period was introduced in the central arm of the figure-8 maze.

The testing phase consisted of 5 consecutive days when mice ran 60 laps a day separated into 6 blocks with three different delays periods (no delay, 2-s delay and 10-s delay) that were each repeated twice. The order at which the different delay blocks were presented was pseudorandomized to ensure that each condition had the same levels of motivation/hunger. All mice followed the same order. After the behavior testing mice were allowed 5-10 days with *ad libitum* food before a microdrive implant surgery was performed. Mice were then allowed 5 days of post-op recovery before food restriction resumed. While tetrodes were lowered into the hippocampus over 6-15 days, mice were trained to run in the figure-8 maze with elastics supporting the tether, and a maximum of 30 laps without intervening delays were performed per day. Once the tetrodes reached the hippocampus, daily recordings with 60 laps and with the different delay conditions commenced. At least 10 days of behavioral data was obtained using the same design as for recording days, even if the microdrive implant failed to produce data (due to a failure of the microdrive to advance, a broken ground, or unstable recordings).

Electrode implant surgery

Tetrodes were prepared by twisting 4 insulated platinum wires (0.017 mm of diameter, California Fine Wire Company) and melting the insulation to bind the four electrodes together. The electrodes were loaded into a 16-channel microdrive[58] and plated with platinum to achieve stable impedances near 200 MΩ. The microdrive was fitted with an optic fiber attached to the tetrode bundle (200 μm diameter optic fiber, Thor Labs) which provided stability and guidance. Mice were anesthetized with 1.5-2% isoflurane vaporized in oxygen in a stereotaxic apparatus. Analgesia was provided by a subcutaneous lidocaine (1%) injection in the animal's head and an intraperitoneal injection of buprenorphine (0.02 mg/kg). Four or 5 small stainless steel anchor screws were positioned in the skull of the animal. A ground screw was positioned touching the left hemisphere cortex (AP -0.7; ML -2.6) and a small circular craniotomy was performed above the hippocampus on the right hemisphere (AP -1.9; ML +1.8). The tetrode tips were slowly inserted 0.4 mm beyond the dorsal surface of the brain. The exposed tetrode wires were protected by a gel (Na-Alginate cured by $CaCl_2$) and a guide cannula, and the microdrive was secured with several layers of dental acrylic to the skull and the anchor screws. A subset of aged mice was implanted with 16-channel silicon probes (Neuronexus A1x16-3mm-50-177-CM16LP). In this case, the probe was directly lowered into the CA1 region of the hippocampus (-1.7 mm from the surface of the brain). A ground wire was positioned on the surface of the cortex in the right hemisphere and a reference wire was positioned in the left hemisphere cortex (AP -0.7; ML -2.6). The reference/ground wires and the probe were then secured in place with dental acrylic. Animals were allowed to recover from surgery in their home cage over a heating blanket until awake.

Electrophysiology recordings

Tetrode advancement started 5 days after the surgery and accrued to a maximum of 0.25 mm per day to retain stability. Recordings were performed only when tetrodes reached hippocampal principal layers (CA1, CA3 and DG) and well isolated clusters could be observed. Neuronal activity was also recorded during short rest periods before and after the behavioral testing for assessing cell stability over time and sparsity of cells, as some cells are silent during running. Only cells that were stable throughout the entire recording session were used for further analysis, and firing rate and spike shape were used to classify recorded spikes as putative principal cells or putative interneurons. Depending on the stability of clusters, tetrodes were advanced at the end of the day to ensure that a different set of cells was recorded the following day. The recordings stopped when all tetrodes had crossed the hippocampal layers or when the end of the drive range was reached (~3 mm). The implanted microdrive was connected to a digital Neuralynx recording system (Neuralynx, Bozeman, MT) through a multichannel, headstage preamplifier. The headstage and multi-wire tether were supported by a system of elastics to counteract their weight. Signals were amplified (5,000-20,000 times) and band-pass filtered (0.6-6 kHz) for spike detection, and spike waveforms above a threshold of 35-50 μV were time-stamped and digitized at 32 kHz for 1 ms. Continuous LFP in the 0.1-900 Hz band was recorded from one of the wires from each tetrode at a sampling rate of 32 kHz. The x-y position of the mouse was tracked at 30 Hz by a video camera mounted above the experimental area. The camera detected a red and a green LED located on either side of the headstage. A maximum of 2 recording sessions that were separated by at least 2 h were performed per day. The number of sessions completed per mouse varied between 4 to 20, depending on (1) the stability of the drive and (2) when tetrodes reached the layer (tetrodes were not independently movable). While we avoided double-counting cells by advancing tetrodes every day, in some cases the same cells could have been included in more than one analysis day.

Histology and tetrode locations

At the end of the recording procedures, mice were anesthetized with isoflurane (4%) and given an overdose of sodium pentobarbital (>30 mg/kg) intraperitoneally. They were then perfused transcardially with Ringer's solution (135 mM NaCl, 5.4 mM KCl, 1.8 mM $CaCl_2$ 1 mM $MgCl_2$ 5 mM HEPES, pH 7.4) followed by 4% paraformaldehyde (PFA, Affymetrix USB). Brains were removed from the skull and post-fixed overnight in 4% PFA at 4 °C. For a subset of mice (part of the aged group) the brain was extracted after the perfusion with cold Ringer's solution and the right hemisphere was then fixed for 48-60 h in 4% PFA. All brains (or hemibrains) were transferred to a 30% sucrose solution for cryopreservation 48 h before sectioning. Coronal sections (40 μm) from the entire dorsal hippocampus were cut with a freezing microtome. Half of the sections were mounted and stained with cresyl violet to identify the small lesions caused by the electrodes, and these locations were then mapped onto the stereotaxic atlas of the mouse brain. The remaining sections were saved for immunohistochemistry. Images were acquired using a virtual slide microscope (Olympus VS120).

Immunohistochemistry

In order to facilitate immunohistological quantifications and colocalization examinations of hAPP with other markers, antigen retrieval and an amplification reaction were used for hAPP detection. Slices were washed and then incubated for 20 min in 70% formic acid for antigen retrieval followed by 3 washes with 1x PBS. To block endogenous peroxidase activity slices were incubated for 1 h with a 3% hydrogen peroxide solution at room temperature (RT) followed by a double blocking step, first with a blocking solution [10% goat serum (NGS) and 0.05% Triton-X in 1x PBS] for 1 h at RT, second with blocking buffer (10% NGS, provided by the ThermoFisher B40932 kit) for 1 h at RT. Slices were then incubated overnight at 4°C with primary antibody [biotin anti-β-amyloid, 1-16 antibody, clone 6E10 (BioLegend) diluted 1:500 in antibody dilution buffer containing 5% NGS and 0.5% Triton-X in 1x PBS]. After overnight incubation and 3 washes for 10 min each with 1x PBS, the slices were incubated with HRP-conjugated streptavidin for 1 h at RT. Amplification reaction was performed for 5 min using the Alexa Fluor 488 tyramide (ThermoFisher B40932 kit) followed by immediate application of the stop reagent for 15 min at RT. Next, the slices were washed 3 times with 1x PBS and incubated overnight at 4°C with primary antibodies for GAD67 (1:500, Invitrogen PA5-21397) and NeuN (1:2000, Sigma-Aldrich ABN91) dissolved in a carrier solution containing 8% NGS and 0.3% Triton-X in 1x PBS. Sections were then washed for 10 min with 1x PBS and incubated with secondary antibodies overnight at 4°C using highly cross-adsorbed Alexa dyes (Invitrogen) diluted 1:1000 in an antibody dilution buffer containing 4% NGS and 0.3% Triton-X in 1x PBS. Sections were washed 3 times in 1x PBS before performing a staining with DAPI (ThermoFisher 62247) at 1:10,000 in 1x PBS for 5 min. After washing 3 times with 1x PBS, slices were mounted with Prolong Gold Antifade (ThermoFisher P36930) mounting media. Overview images were acquired with a custom-built Thorlabs EpiCerna fluorescence microscope (4x objective). Immunohistochemistry overlap quantifications were performed on confocal image z-stacks acquired using a Leica SP5 confocal microscope (20x objective). Quantification of hAPP expression was done in individual planes obtained from a confocal microscope using 40x magnification lenses (Olympus FluoView, FV1000).

Spike sorting and cluster quality

A customized version of the spike sorting software MClust, MATLAB 2009b (Redish, A.D. Mclust. https://redishlab.umn.edu/mclust) was used for spike sorting. Clustering was performed manually in two-dimensional projections of the parameter space using waveform amplitude, waveform energy and the peak-to-valley difference. For a given cluster unit, the same boundaries were used across the rest and behavioral task segments of a recording session. Single units were excluded from analysis if they were not separable from either the noise or other single units. To ensure stability all units included in the study were required to have spikes in both the pre and post-behavioral resting sessions, while they were not required to have spikes during the behavior blocks. Cluster quality

was assessed by calculating the L-ratio and isolation distance[59] (Figure S2B) for each cluster during behavior. The L-ratio is calculated by dividing L by the number of spikes within the cluster, where L is calculated from the sum of 1 minus the Chi-square cumulative distribution function of the Mahalanobis distance of the spikes outside the cluster.

Unit classification

Isolated units were classified using a set of criteria applied to their average firing rate and peak-valley ratio of their spike waveform (Figure S2C) calculated from the entire session (behavior, pre- and post-resting periods). The criteria definitions were chosen to accommodate possible changes in rate or spike properties that could occur as a result of our genetic manipulation. Putative principal cells were defined as units with (i) a peak-valley ratio above 0.9, (ii) an average firing rate below a threshold defined by a slope [0.4*mean firing rate with a offset of -(peak-valley ratio + 1)] that allowed higher average firing rates for cells with higher peak-valley ratio, and (iii) a maximum mean firing rate of 10 Hz. The classification of putative principal cells was the same for recordings in CA1 and CA3/DG.

The vast majority of putative interneurons in the CA1 region were recorded within *stratum pyramidale*, whereas recordings in the CA3/DG regions also included some units recorded from the hilar region. Therefore, putative interneurons were classified separately for CA1 and CA3/DG recordings in order to include the more diverse classes of interneurons in the latter regions. Putative interneurons in CA1 were defined by the following criteria: (i) a firing rate of 5-60 Hz, (ii) a peak-valley ratio below 2, and (iii) a ratio of firing rate to peak-valley ratio above a slope [0.1*mean firing rate with an offset of -(peak-valley ratio - 0.5)] which includes interneurons with lower firing rates (> 5 Hz) if they have a low peak-valley ratio, a known feature of interneurons. Units recorded in CA3/DG were classified as putative interneurons if they (i) were not classified as principal cells, (ii) had a firing rate of 5-60 Hz, and (iii) had a maximum peak-valley ratio of 2. Units that did not fulfill the inclusion criteria were excluded from further analysis (Figure S2C).

LFP analysis

Local field potentials (LFPs) obtained from the hippocampus were referenced to a ground screw with microdrive recordings or to a reference wire with silicon probe recordings (both were located at the same coordinate). For each recording session the selection criterium for the tetrode for LFP analysis was that it had clearly defined clusters and the highest amplitude of sharp-wave ripples (SWR). For the recordings performed with the silicon probes, the selected channel was the one immediately below the channel registering the highest SWR power. Raw LFP signals were downsampled to 2 kHz and the spectrogram was calculated for frequencies of 2-300 Hz using a Morlet wavelet transformation (MATLAB package).[60]

Normalized spectrograms

To be able to analyze oscillations without preselecting different frequency ranges, we first normalized the LFP signal in the working memory task to the LFP recorded during rest periods in the home cage (running speed < 2 cm/s) before the start of the memory task (Figure S5A–S5C). Normalized spectrograms were calculated by dividing spectrograms by the power spectral density (PSD) of the resting period (r1) on the same recording day, so that normalized spectrograms for the behavioral task reflect amplitudes as multiples of the amplitude during rest. This normalization was considered more rigorous than a Z-score or a 1/f correction as it (i) is independent of the activity of the mice during the delay and allows for a much better comparison between mice (as some quietly wait for the barrier to be lifted while others move between the two barriers), (ii) provides an internal baseline that does not depend on the exact location of the recording or how good we can fit an exponential to the signal, and (iii) normalizes equally between high and low frequencies (the variation of signal standard deviations is higher at lower frequencies).

Average normalized spectrograms

An average normalized spectrogram was calculated over all laps per session using a linearized path in which each bin represents the average time spent in each region of the maze, and all sessions per mouse were combined.

Definition of frequency bands

PSDs that were derived from the normalized spectrograms of control mice were used for the unbiased identification and definition of LFP bands that were relevant during different phases of the memory task (Figure S5C). Boundaries of five LFP bands were evident – delta (2-6 Hz), theta (6-12 Hz), beta (14-26 Hz), low gamma (26-50 Hz) and high gamma (50-120 Hz).

Quantification within each frequency band

For each of the five frequency bands and maze segments (i.e., return, delay, stem, choice, reward and stem+choice), the most prominent peak frequency was identified using the average PSD from normalized spectrograms in which all correct-turn trials of one behavioral session were included. The power in each frequency band was defined as the power at the peak frequency. Peak frequency and power were averaged over all sessions per animal. Peak frequency and power were also calculated using the PSDs from raw spectrograms, but in contrast to the reliable detection of peak frequencies from PSDs generated with normalized spectrograms, we could in many animals not consistently detect peaks at higher frequencies (Figures S7 and S12; Tables S10 and S14).

Visualization of spectrograms

For visualization in figure panels, the parsed spectrograms were resized to match the average time duration that all the animals spent in this region, which allowed for averaging across trials of different durations. Spectrograms were averaged first over trials of each animal and then over all animals within an age group and genotype (young adult/aged, CA3-APP/control). The average spectrogram for each group is shown.

Firing properties of single units

Average firing rate was calculated from the total number of spikes that occurred during the entire session (three delay conditions and two rest sessions). No speed threshold was applied. *Speed score* was calculated by first calculating the instantaneous firing rate in 250 ms bins for spikes that occurred when the animal was running at a velocity above 2 cm/s. Pearson's correlation between instantaneous firing rate and instantaneous velocity was then calculated to obtain the speed score of each cell. The average of the three delay conditions was weighted by the number of spikes of each session (d0, d2, d10). *Active cells* were defined as cells with a firing rate above 0.1 Hz during behavior (approximately 60 spikes per ~10 minute-session). *Bursting index* was defined as the total number of spikes occurring in bursts (interspike interval <6 ms) divided by the total number of spikes.[61]

Place cell analysis

The path of the animal in the figure-eight maze was linearized and binned into 76 spatial bins of 2.5 cm x 2.5 cm. A lap started and ended at the reward location. Right and left starting laps were analyzed separately. Because control mice have very few incorrect laps and because the memory deficit in CA3-APP mice was most pronounced with the 10-s delay, only correct laps recorded from the 10-s delay condition (d10) were used. A binned rate map was calculated for each cell by dividing spikes by time spent in each bin and smoothing with a one-dimensional version of the boxcar filter. *Place cells* were defined as cells with a peak firing rate of $\geq$ 3 Hz in at least one spatial bin and at least one place field between 12.5 cm and 70 cm. The *place field(s)* of a cell were defined by including the space before and after the peak in which the firing rate remained above 20% of the peak firing rate. The start and end points (20% of the peak value) of the place field were determined on up-sampled (linearly interpolated) data. To determine the *number of place fields per cell* and to avoid counting peaks in the central arm (where left and right turns overlap) twice, place fields occurring in the central arm (delay + stem) with an overlap above 25% of the place field extent were removed for the turning direction with the lower place field peak firing rate. The *peak firing rate* of a place cell was defined as the spatial bin with the highest rate value. *Spatial information*, defined as the information density per spike (I), was calculated as previously described[35] using the average rate and occupancy maps for left and right laps. The following formula was used:

$$I = \sum_{i=1}^{N} p_i \frac{F_i}{F} \log_2 \frac{F_i}{F}$$

where *pi* is the probability of occupancy in bin *i*, *Fi* is the mean firing rate for bin *i* and *F* is the mean firing rate.

Place cell spatial correlations

All spatial correlations were calculated from the linearized rate maps of correct laps during the 10-s delay condition (d10). *Trial by trial correlation* as a measure of stability was calculated as a Pearson's cross-correlation of the firing rates between every combination of trials with the same turn direction. Spatial bins corresponding to the delay area were removed. To account for cells with a place field only on one side of the maze, the correlation was calculated separately for left-turn and right-turn laps, and the maximum correlation value was used. The *correlation across sides* was calculated as the average Pearson's cross-correlation between the rate maps of left-turn and right-turn laps. Only bins corresponding to the non-overlapping return arms were used. *Splitter cells* were defined as place cells where the following criteria were fulfilled for at least two consecutive spatial bins (5 cm): (i) the firing rate was at least 5 Hz and (ii) at least twice as high as for the opposite turn direction. This analysis excluded the final segment of the stem, where the animal's path started to diverge and where sensory inputs may therefore differ across laps with different turn directions. The splitter acuity/selectivity index was calculated from the inverse of a Pearson's correlation between the average rate maps of left-turn and right-turn laps along the delay and the central arm [S = (1/(r+1))-0.5], where a larger value indicates stronger distinction between left and right turns.

Temporal properties of single units

To determine the theta modulation (spike oscillation frequency and theta modulation strength) of each unit, the Fourier transform of the autocorrelation of all spikes was calculated (time resolution: 5 ms) and filtered in the theta band from 6 to 14 Hz. Based on spike and LFP timestamps, the theta phases at the time of every spike were interpolated. Using circular statistics, we calculated the mean vector length and the mean phase of the spikes of each cell and the significance of theta modulation.

Phase precession and sequence compression

For each place cell, phase precession was calculated using trains of activity (spike interval <500 ms and including at least 5 spikes). The slopes of each spike train (significant or not) were then used to obtain the median value of phase precession. For the sequence compression analysis, 2D place fields were defined in the maze if there were a minimum number of 8 bins above threshold and if at least one bin had a peak rate of > 3 Hz (2.5 cm by 2.5 cm bins were included if the rate in the bin was at least 0.3 Hz). Minimum overlap between fields was 15%, and place fields overlapping across the delay area were excluded, as we could not establish the earliest place field. Spatial distance between place fields was the linear distance between the centers of mass of two place fields. Crosscorrelograms were generated for all overlapping cell pairs (bin size: 7.5 ms, from -3 s to 3 s). The *real time* was defined as the highest peak in the crosscorrelogram, while the theta time was defined as the highest peak within the -100 ms to +100 ms interval. Correlations between distance, real time and theta time were performed using Pearson's correlation tests.

QUANTIFICATION AND STATISTICAL ANALYSIS

All data collection and clustering of units was done blind in regards to the genotype of the subjects. All statistical tests were conducted using GraphPad Prism8, and the details and parameters of the tests used are provided in Tables S2–S17. Normality of the data was tested using the Shapiro–Wilk test. When data was normally distributed, t-test or ANOVA were used to compare means of two or more groups, respectively, and otherwise, non-parametric tests were used (Mann-Whitney rank-sum test or Kruskal-Wallis test). Post-hoc tests were corrected for multiple comparisons (two-way ANOVA with Sidak's multiple comparisons correction and Kruskal-Wallis test with Dunn's multiple comparison correction). Wilcoxon rank-sum test was used to evaluate difference from reference value, and Kolmogorov-Smirnov test to compare distributions. Pearson correlation test was used to calculate correlations for normally distributed data, and the Spearman correlation test for non-parametric data. No outlier analysis was performed and no data points were excluded.